



Particle mass flow determination in dust-laden supersonic flows by means of simultaneous application of optical measurement techniques

Dirk Allofs¹ · Dominik Neeb¹ · Ali Gülhan¹

Received: 30 July 2022 / Revised: 20 December 2022 / Accepted: 29 December 2022 / Published online: 21 February 2023
© The Author(s) 2023

Abstract

Particle mass flow rate and particle mass concentration are key parameters for describing two-phase flows, especially for particle-induced heating augmentation analysis. This work addresses the question of how accurate particle mass flow rate can be determined with three non-intrusive measurement approaches, based on shadowgraphy, particle tracking velocimetry (PTV), and scattered light intensity, in supersonic flows. In terms of shadowgraphy and PTV, the particle mass flow rate was determined by measuring individual particle characteristics, namely particle size, velocity, and density, as well as the measurement volume. The presented shadowgraphy procedure is based on the commercial LaVision DaVis software and additional shadowgraphy corrections. Multiple tests were conducted in the experimental test facility GBK of DLR with varying flow conditions, at a Mach number of 2.1, unit Reynolds number (Re_∞) ranging from $5e7$ 1/m to $1.5e8$ 1/m, total temperature (T_0) ranging from 303 to 544 K, and particle materials, namely Al_2O_3 , MgO, and SiO_2 , in the size range of 1 to 60 μm . Particle size distributions of Al_2O_3 and MgO particles could be reproduced with shadowgraphy quite well, while the PTV procedure resulted in non-similar distributions. Pycnometer measurements indicated MgO particle density to be significantly lower than reference values. A DaVis parameter variation analysis resulted in a particle mass flow rate uncertainty of shadowgraphy of up to 30%. The particle mass flow rate uncertainty of PTV is approx. 76%, and the respective uncertainty of scaled PTV and scattered light intensity approach is 28%. The particle mass flow rate, measured with shadowgraphy, is 58% higher than those of the semi-axisymmetric scattered light intensity approach, which can be explained by a higher particle concentration at the injection plane.

Abbreviations

BiThr	Shadowgraphy binarization threshold [%]	$d_{p \text{ min, full}}$	Shadowgraphy's minimum detectable particle size which can be fully detected [μm]
CE	Count efficiency [–]	$d_{p \text{ True}}$	True size of calibration dots [μm]
d_{nozzle}	GBK nozzle exit diameter [mm]	d_{shadow}	Measurement volume thickness [mm]
DOF	Depth-of-Field	$d_{\text{shadow CE=1}}$	Shadowgraphy measurement volume thickness for which CE=1
d_p	Particle diameter [μm]	$d_{\text{shadow minGS}}$	Shadowgraphy measurement volume thickness, limited by the minimum GS boundary [mm]
$d_{p \text{ detected}}$	Detected particle size with DaVis, without additional size correction [μm]	FOV	Field-of-View
$d_{p \text{ min}}$	Shadowgraphy's minimum detectable particle size [μm]	GBK	Multi-phase flow facility ('Gemischbildungskanal')
		G_p	Particle mass flow rate [kg/m^2s]
		$G_{p \text{ PTV}}$	Particle mass flow rate, based on PTV data [kg/m^2s]
		$G_{p \text{ PTV scaled}}$	Particle mass flow rate, based on PTV data, scaled to Mp Nozzle [kg/m^2s]

✉ Dirk Allofs
dirk.allofs@dlr.de

¹ Supersonic and Hypersonic Flow Technologies Department, DLR, Cologne, Germany

G_p scatter	Particle mass flow rate, based on scattered-light intensity [kg/m ² s]
G_p scatter qual.	Particle mass flow rate, based on scattered light intensity, qualitative [kg/m ² s]
GS	Gradient slope [%/px]
IQR	Interquartile range
Minimum GS offset	Limiting gradient slope for infinitesimal small detected particle diameters [%]
M_p calc	Calculated total particle mass
M_p collected	Total particle mass collected with the injection collection probe [g]
M_p nozzle	Total particle mass passing the nozzle
NorRad	Shadowgraphy normalization radius [px]
p_0	Stagnation pressure [MPa]
PIV	Particle Image Velocimetry
PTV	Particle Tracking Velocimetry
Re_∞	Unit flow Reynolds number [1/m]
T_0	Flow stagnation temperature [K]
t_{meas}	Evaluation time in which shadowgraphy and PTV images are considered for processing [s]
VOI	Volume-of-Interest
V_p	Mean particle velocity [m/s]
z_{PTV}	Laser light sheet thickness [mm]
γ	Specific heat ratio [-]
$\Delta M_{seeding\ device}$	Mass difference of seeding device before and after each run [g]
Δt	Double-pulse time separation [ns]
ρ_p	Particle density [kg/m ³]

1 Introduction

In a collaboration between the NASA Entry Systems Modeling (ESM) project and the Supersonic and Hypersonic Technologies Department of DLR, supersonic two-phase flows and its effects on surface heating and erosion are investigated. Key parameters, describing those two-phase flow effects, are the particle mass flow rate (G_p) and particle mass concentration (Bakum 1970; Fleener and Watson 1973; Kudin et al. 2013; Polezhaev et al. 1992). In literature concerning particle-induced heating augmentation, the qualitative G_p distribution across supersonic nozzle exits was determined with the help of dust catcher probes (Kudin et al. 2013; Polezhaev et al. 1992), light attenuation correlation (Kudin et al. 2013) or scattered light correlation (Vasilevskii and Osipov 1999), while its quantitative value was defined by total particle mass loss measurements of the seeding system before and after each test run (Dunbar et al.

1974; Fleener and Watson 1973; Vasilevskii and Osipov 1999). While dust catcher probes were only used during calibration tests and only provided time-integrated particle mass values, the scattered light method was used to account for temporal changes, as they were reported for the particle mass flow rate in (Fleener and Watson 1973; Vasilevskii and Osipov 1999). In (Vasilevskii and Osipov 1999), it was assumed that the scattered light signal is proportional to the particle mass flow rate.

To the best knowledge of the authors, there is no study measuring G_p with the help of the simultaneous and individual determination of particle number density, size (d_p), and velocity (V_p) within supersonic flows up to now. To fill this gap, two measurement procedures were introduced in (Allofs et al. 2022), based on shadowgraphy and particle tracking velocimetry (PTV). However, several issues and limitations came up in that work: investigation of only one flow condition and only one particle material, a relatively high amount of invisible particle mass flow rate of up to 18%, ambiguity of particle density, and no quantitative comparison of measured particle mass flow rates to other measurement approaches. In that work, shadowgraphy particle detection was performed with the help of LaVision DaVis V10.1 software. As discussed in (Kapulla et al. 2008), several detection settings of the DaVis software can have a significant effect on the detected particle size and, hence, on the particle mass flow rate. As mentioned in (Legrand et al. 2016; Senthilkumar et al. 2020), a check of how many particles are detected within the shadowgraphy measurement volume is recommended. These two aspects - influence of particle detection settings on G_p and the particle detection rate, are missing in the uncertainty analysis made in (Allofs et al. 2022).

The question to be answered in this work is as follows: How accurate can the particle mass flow rate be measured with the measurement procedures, based on shadowgraphy and PTV, in different supersonic flow conditions and for particle sizes in the range of approx. 10–100 μm ? To answer this question, a three-step approach was considered, which can be seen as a guideline of this work:

- Qualitative comparison of particle size distributions with reference data
- Determination of G_p measurement uncertainty
- Quantitative comparison of particle mass flow rates in supersonic flows

Experiments at several supersonic flow conditions and using different particle materials were carried out in the experimental test facility GBK of DLR Cologne. Shadowgraphy's and PTV's G_p uncertainty was determined with the help of linear propagation theory. The influence of the DaVis particle detection settings, especially on the shadowgraphy's

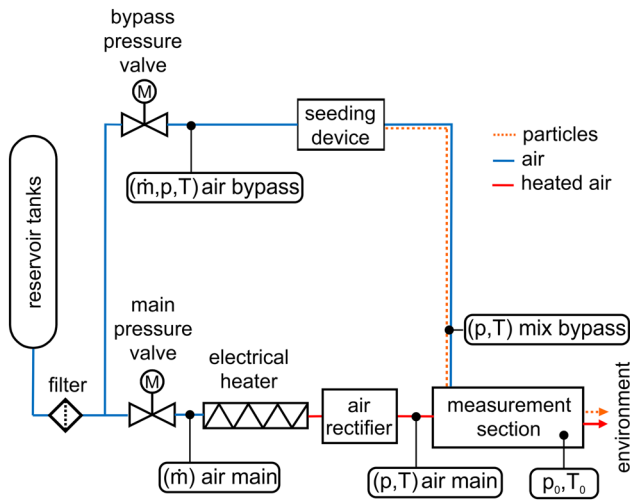


Fig. 1 Sketch of the GBK facility, taken from (Allofs, Neeb and Gülhan 2022)

G_p uncertainty, was investigated. All reported issues from (Allofs et al. 2022) were addressed, and the additional correction of shadowgraphy data was extended to account for the particle detection rate and particles down to $3 \mu\text{m}$.

It is common to use intrusive methods to achieve integrated reference particle mass flow rate distributions (Fleener and Watson 1973; Kudin et al. 2013; Polezhaev et al. 1992). The application of simple dust catcher probes was also tested in preliminary tests in the GBK facility. Almost all particles were sucked out of these steel wool-filled probes during the facility’s shut-down phase. To compensate this lack of reference measurements, particle mass flow rates, based on shadowgraphy and PTV, were instead compared quantitatively to data based on scattered light intensity signals and total particle mass loss measurements of the seeding system, as it was used in a similar manner in (Vasilevskii and Osiptsov 1999).

This work is organized as follows: First, the experimental test setup is explained, followed by the descriptions of the shadowgraphy, PTV, and scattered light intensity approach for particle mass flow rate determination. Then, the results of all relevant sub-measurements are presented. In the end, results are discussed, following the above-mentioned three-step guideline.

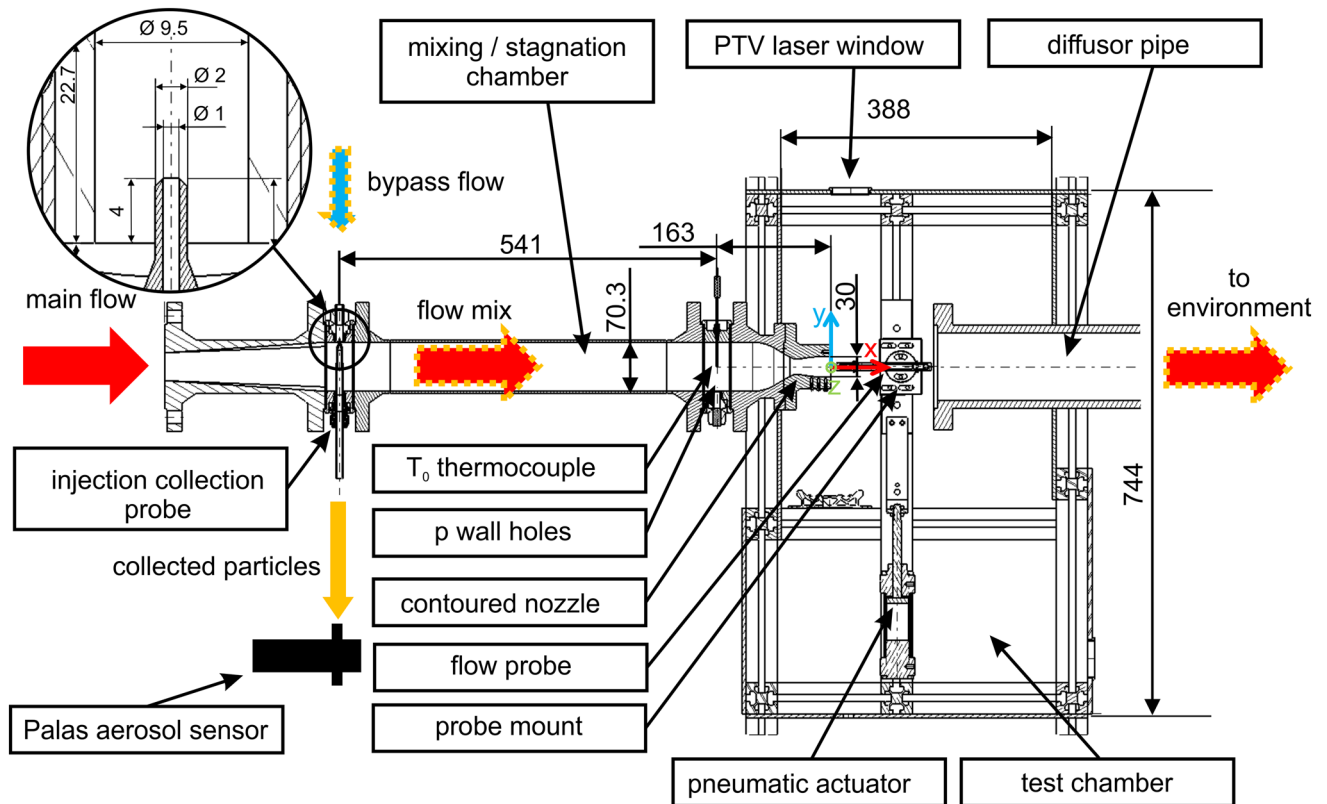


Fig. 2 Sectional side view of the GBK measurement section, dimensions given in mm

2 Methods

In the following, first the experimental setup of the test facility, the optical setup of all cameras, the particles as well as the investigated test conditions are described. Then, three different approaches for the determination of particle mass flow rate are explained. For these approaches, several sub-analyses are required which are depicted in the respective subsections.

2.1 Test facility setup

Tests were performed in the multi-phase flow facility (GBK), which is a blow down facility, using high-pressurized air from reservoir tanks. The maximum design pressure of the GBK facility is 5.4 MPa, while the maximum design temperature is 800 K. Two different air flows can be controlled automatically: a heatable pure air flow, named ‘main’ flow, and an unheated particle-laden flow, named ‘bypass’ flow in the following. Particles were seeded with an in-house developed seeding device. The GBK flow can be fully determined with the help of several temperature, pressure, and air mass flow sensors at measurements points in the main and the bypass flow section. An overall sketch of the GBK facility is given in Fig. 1.

In this investigation, the main air flow and the bypass air flow were mixed in the measurement section. The complete measurement section is shown in Fig. 2. It consisted of a cross section adapter, an injection adapter, a stagnation

chamber, a de-Laval nozzle, a test chamber, and a flow diffusor.

In the injection adapter, the heatable main flow was mixed with the cold two-phase bypass flow. Here, a circular conical particle injection collection probe was located. A closed container was mounted at the outlet of the injection collection probe; in selected tests, a Palas aerosol sensor welas 2070 HP or 2300 HP, connected to a Palas Promo 3000 HP, was installed. Due to its time-resolved measurement ability, the aerosol spectrometer was used to check the absence of particle seeding during the facility’s heat-up and shut-down phase. The maximum particle concentration for both sensors was $1e6$ particles/cm³ and $4e4$ particles/cm³, respectively. Considering the spectrometer’s maximum design pressure of 1 MPa and its maximum design temperature of 393 K, it was only installed for tests with lower stagnation pressures (p_0) and flow stagnation temperatures (T_0). A constant air volume flow of 5 l/min was required for accurate particle size determination, which was controlled by the spectrometer. The internal velocity calibration of the spectrometer was performed, while the flow of the facility was running. Special calibration particles, provided by Palas, were used for size calibration. It is assumed that the choice of spectrometer and closed container at the injection collection probe did not affect the nozzle flow. Particles were collected with the injection collection probe to check whether particle total mass flow can be predicted only with the collected particle mass, while the aerosol

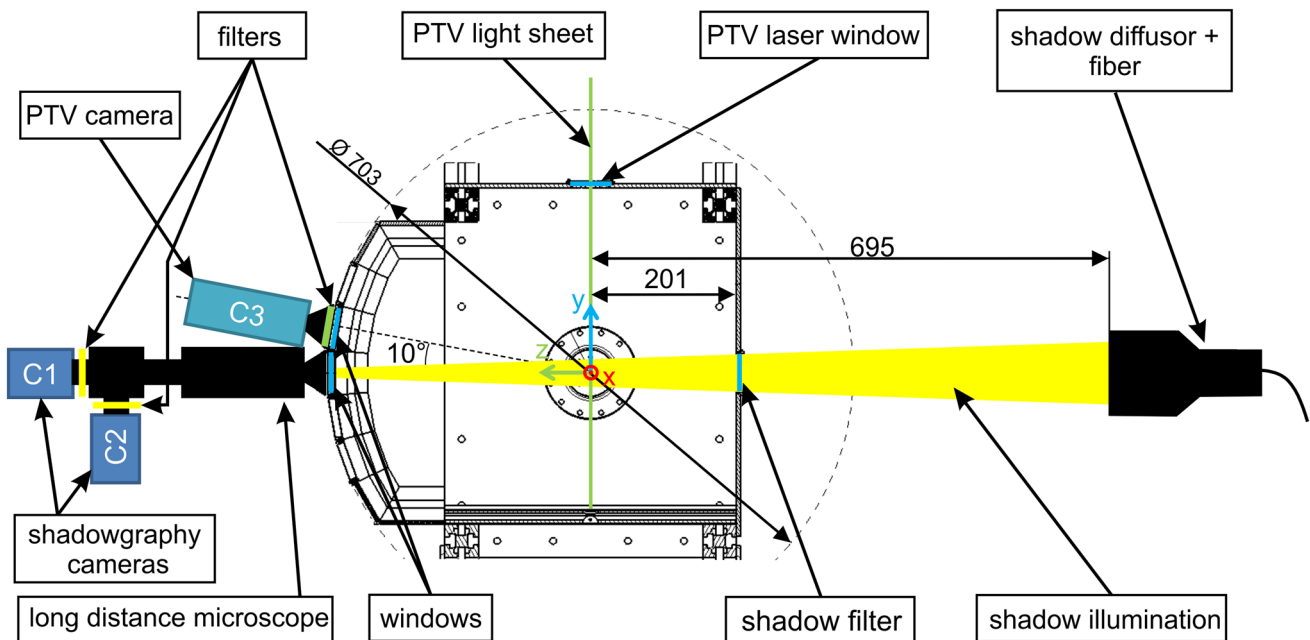


Fig. 3 Front view on the PTV and shadowgraphy setup, dimensions given in mm

spectrometer was used to check the absence of particle seeding beyond the measurement time.

Behind the injection adapter, a stagnation chamber with a diameter of 70.3 mm and an ideal-contoured $Ma=2.1$ de-Laval nozzle with a nozzle exit d_{nozzle} of 30 mm were placed. The nozzle flow was directed into a diffusor, located at the end of a test chamber. The flow stagnation temperature was measured with a 1.1-mm-diameter type K thermocouple in front of the nozzle. The stagnation pressure was reconstructed by means of the wall pressure close to the T_0 sensor, to avoid particle deposit in a Pitot tube. The operation range of the described GBK setup is given in (Allofs, Neeb and Gülhan 2022). The GBK facility can run continuously, because of its small size.

An almost hemispherical-shaped axisymmetric probe was inserted into the flow, which was equipped with a coaxial thermocouple, whose data were not considered in this work. The probe allowed to investigate similar flows and similar particle mass flow rates as expected in future particle-induced heating augmentation tests. The probe tip was made of stainless steel (1.4539). Its diameter was 12 mm and its length, from tip to its mount, was 60 mm. During the test series, it was observed that the distance between probe tip and nozzle exit has varied between 4 and 6 mm, which is caused by thermal expansion of the nozzle.

2.2 Optical setup

The non-intrusive measurement technique setup was similar to those described in (Allofs, Neeb and Gülhan 2022). It included a shadowgraphy system and a particle tracking velocimetry (PTV) setup. An overview of the optical setup is sketched in Fig. 3.

While shadowgraphy provided accurate particle size and velocity data in a small central field of view (FOV), the PTV setup was used for achieving particle velocity data across the entire facility nozzle exit. Both techniques measured the particle velocity with the similar principle as particle image velocimetry (PIV): Each camera recorded two images. Particles were illuminated with a double-pulse light source with a pre-defined time separation (Δt) between those two pulses. A cross-correlation algorithm was used to detect the particle displacement between both pulses. The particle velocity is the ratio between its displacement and time separation between the two light pulses.

The high-magnification shadowgraphy system consisted of two LaVision Imager sCMOS cameras (named C1 and C2, respectively), having a pixel size of $6.5 \mu\text{m}$. A long-distance microscope K2 Distamax of Infinity Photo-Optical Company was equipped with a CF-1b lens, a 'Zoom Module,' and an optical beam splitter so that both cameras used the same optics. To avoid double exposure by the 100-Hz laser system, only a central sensor area of $1060 \times 2560 \text{ px}^2$

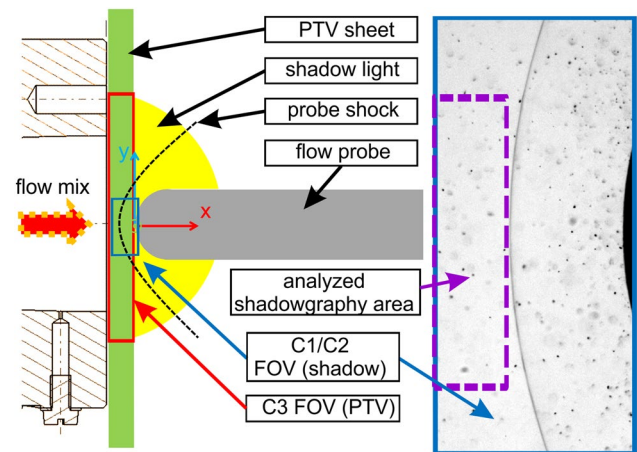


Fig. 4 Sketch of FOVs: shadowgraphy FOV (blue), PTV FOV (red). Only data in front of the shock are evaluated (shadowgraphy: purple)

Table 1 General flow constants

Parameter	Unit	Value
Flow		
γ	–	1.4
R	$\text{m}^2 / (\text{s}^2 \text{ K})$	287.058
Ma	–	2.1

for C1 and C2 was used, ensuring a double-image rate of 50 Hz for each camera. The cameras were recording one after the other, resulting in a shadowgraphy double-image recording rate of 100 Hz. The optical magnification was increased to 327.5 px/mm for C1 and C2 by increasing the optical amplification level of the 'Zoom Module.' The aperture control of the long-distance microscope was set to the middle position, resulting in an aperture opening of approx. 17 mm in diameter. C1 and C2 were equipped with a 564-nm long-pass filter. The working distance between lens and focus plane was 361 mm. The resulting shadowgraphy FOV was $3.2 \times 7.8 \text{ mm}^2$. Particle shadow displacements were between 40 and 80 px. The depth-of-field (DOF) was less than 6 mm for particles smaller $60 \mu\text{m}$.

The PTV camera (named C3 in the following) was a PCO 1600 with a Nikon Nikkor tele lens. Its pixel size was $7.4 \mu\text{m}$ and the lens aperture was set to $f/11$. The resulting optical magnification was 40.6 px/mm. A Scheimpflug adapter was used to compensate the angle of 10° between vertical focus plane and camera. The working distance between lens and focus plane was similar to the shadowgraphy system. Distancing rings provided the required short focal length. The active sensor pixel area was reduced to $168 \times 1600 \text{ px}^2$ to increase the camera's double-image recording rate up to 50 Hz. The 50-Hz image rate avoided double exposures by the 100-Hz laser system. The resulting

Table 2 Test matrix, sorted by particle material, T_0 , and p_0

synonym	p_0	T_0	\dot{m}_{main}	p_{main}	T_{main}	$\dot{m}_{\text{mix by}}$	$p_{\text{mix by}}$	$T_{\text{mix by}}$	material	t_{meas}	aerosol spectrometer/collection
[–]	[MPa]	[K]	[g/s]	[MPa]	[K]	[g/s]	[MPa]	[K]	[–]	[s]	[–]
A-11-1	0.594	303.3	496.2	0.600	303.7	29.8	0.602	285.8	Al ₂ O ₃	11.51	Palas: 2070 HP
A-12-1	0.958	303.5	798.7	0.958	302.9	45.4	–*	290.9	Al ₂ O ₃	11.51	Palas: 2070 HP
A-13-1	1.289	303.8	1084.2	1.301	304.5	64.4	1.303	285.6	Al ₂ O ₃	11.51	Collection container
A-14-1	1.686	304.2	1427.8	1.702	304.9	84.4	1.315	287.9	Al ₂ O ₃	11.52	Collection container
A-22-1	0.951	338.5	762.5	0.961	342.6	46.3	0.962	289.9	Al ₂ O ₃	11.51	Collection container
A-22-2	0.950	338.2	746.0	0.959	342.2	46.6	0.959	290.1	Al ₂ O ₃	14.31	Collection container
A-31-1	0.593	374.4	444.6	0.600	381.9	26.6	0.599	293.2	Al ₂ O ₃	11.51	Collection container
A-31-2	0.594	373.3	451.3	0.601	381.5	27.0	0.600	294.0	Al ₂ O ₃	14.33	Collection container
A-32-1	0.952	374.7	719.2	0.961	382.3	45.5	0.960	290.9	Al ₂ O ₃	11.51	Palas: 2070 HP
A-32-2	0.952	374.5	716.8	0.962	381.5	45.1	0.962	292.7	Al ₂ O ₃	11.53	Collection container
A-33-1	1.287	373.2	973.3	1.299	379.1	62.7	1.300	293.0	Al ₂ O ₃	11.53	Collection container
A-33-2	1.286	373.2	972.1	1.300	380.3	63.2	1.300	292.0	Al ₂ O ₃	14.31	Collection container
A-34-1	1.682	373.0	1273.4	1.699	378.7	82.7	1.698	292.5	Al ₂ O ₃	11.51	Collection container
A-34-2	1.686	373.4	1268.9	1.702	381.5	83.6	1.703	292.4	Al ₂ O ₃	14.31	Collection container
A-42-1	0.952	473.6	633.2	0.961	492.3	46.1	0.963	292.3	Al ₂ O ₃	14.31	Collection container
A-52-1	0.952	544.9	588.5	0.961	573.5	45.5	0.962	293.3	Al ₂ O ₃	17.80	Collection container
S-31-1	0.593	374.8	449.2	0.600	383.1	26.7	0.599	292.3	SiO ₂	11.51	Palas: 2300 HP
S-32-1	0.952	374.0	723.7	0.962	382.2	45.6	0.961	289.7	SiO ₂	11.51	Palas: 2300 HP
S-33-1	1.288	373.6	973.9	1.301	380.7	63.2	1.301	289.5	SiO ₂	11.53	Collection container
M-31-1	0.594	373.7	449.2	0.600	383.1	27.6	0.600	290.1	MgO	11.53	Collection container
M-32-1	0.950	373.5	720.5	0.959	380.7	45.6	0.959	291.7	MgO	11.51	Palas: 2070 HP
M-33-1	1.290	373.7	981.8	1.303	381.5	63.0	1.303	288.9	MgO	11.51	Collection container
M-34-1	1.684	373.3	1267.4	1.701	380.3	82.9	1.701	290.4	MgO	11.51	Collection container

*Defective sensor

FOV was $4.1 \times 39.4 \text{ mm}^2$. A 532-nm band pass filter was placed between focus plane and camera lens. C3's particle displacements were between 5 and 10 px.

The PTV and shadowgraphy illumination source was a 'SpitLight DPSS 250 PIV' laser system of InnoLas Laser GmbH, generating two light pulses with a time separation Δt of 400 ns at a repetition rate of 100 Hz. An additional photodiode was used to control and to correct this time separation. The timing of laser and cameras as well as the camera data acquisition was controlled by a PTU-X timing unit of LaVision and the LaVision DaVis software V10.1.

The energy for shadowgraphy and PTV illumination was controlled with a set of half-wave plates and beam splitters. A shadow diffusor of Dantec Dynamics GmbH was implemented for background illumination, providing short pulses with a maximum illumination area of 112 mm in diameter. The diffusor was fed with light from the laser. The shadow diffusor was placed 695 mm away from the nozzle axis.

The PTV light beam was generated by one cylindrical lens with focal length of 500 mm. This lens was placed ahead of the particle section in order to direct the PTV illumination vertically from top to bottom. The PTV light sheet

was around 5 mm wide in x-direction and parallel to achieve homogenous illumination intensity across the nozzle. The laser sheet thickness was determined by an additional calibration (see Sect. 2.9). As suggested in (Allofs, Neeb and Gülhan 2022), the laser light intensity was optimized to decrease saturation effects of large particles in the PTV recordings.

In Fig. 4, the FOVs are sketched: C3's FOV (red rectangle) covered the entire nozzle exit flow, whereas C1 and C2's FOV (blue rectangle) were used for high-resolution image acquisition on the symmetry axis. For PTV and shadowgraphy, the data in front of the probe bow shock were evaluated to exclude particle deceleration behavior. The final areas of data evaluation were $1 \times 4.8 \text{ mm}^2$ (purple rectangle) and $1 \times 30 \text{ mm}^2$, for shadowgraphy and PTV, respectively. The origin of the coordinate system was located at the probe tip.

2.3 Particles

Three different particle materials were used for seeding, namely alumina (Al₂O₃), magnesium oxide (MgO), and silica (SiO₂). The selected Al₂O₃ and MgO particles offered a

significant number of particles larger than 10 μm, which was the smallest fully recognizable particle size of the implemented shadowgraphy system (see Sect. 3.5). The MgO material was taken from Lehmann&Voss GmbH and was additionally sieved to decrease the number of particles smaller than 10 μm, so that the relative number of particles larger than 10 μm increased. SiO₂ was chosen not only because of its significant lower density (see Sect. 3.2), but also because of its relevance for Martian atmosphere simulations in future studies.

Only for the Al₂O₃ and the MgO particles externally analyzed particle size distributions by Microtrac GmbH were available. These data were achieved with a dynamic image analysis device ‘PartAn SI.’ For these measurements, both materials were diluted into water to reduce agglomeration effects. Additionally, MgO particle measurements were also taken in air, resulting in particle size distributions very similar to those measured in wet dilutions. For the SiO₂ particles, no reference size data from Microtrac could be given.

2.4 Test conditions

A total of 23 tests were performed. While the nozzle contour and the resulting Mach number remained constant, T₀, p₀, and particle material were varied. The unit Reynolds number of the flow (Re_∞) ranged from 5e7 1/m to 1.5e8 1/m. The general flow constants can be found in Table 1. An overview of all tests is given in Table 2, where the tests are sorted by particle material, T₀, and p₀. The subscript ‘main’ stands for the heated main flow, while the subscript ‘mix by’ stands

for the particle-laden bypass flow. The measurement locations are sketched in Fig. 1. The reference flow condition was T₀ = 373 K and p₀ = 0.96 MPa. Four different p₀ levels, namely 1: 0.6 MPa, 2: 0.96 MPa, 3: 1.3 MPa, and 4: 1.7 MPa, and five different T₀ levels, namely 1: 303 K, 2: 338 K, 3: 373 K, 4: 473 K, and 5: 545 K, were tested with Al₂O₃ particles. For the other materials, only the variation in p₀ was performed. These conditions were selected to cover the entire GBK operation range. A synonym was defined for each run in the form: material - temperature level/pressure level - test run repetition. For example, the synonym ‘A-32-1’ stands for the run with Al₂O₃ particles, on the third temperature level of 373 K, on the second pressure level of 0.96 MPa, first repetition. The active seeding time was set to 10 s. Considering a recording rate of 100 Hz, 1000 shadow images were assumed to be enough for proper particle data statistics. The probe was inserted into the flow for 5 s within the seeding time. For every run, the evaluation time in which shadowgraphy and PTV images were considered for further processing t_{meas} is given in Table 2. This time was slightly longer than the active seeding time due to the delay of particles running through the facility.

2.5 Determination of particle mass flow rate

Assuming spherical particles and a constant particle density ρ_p for all particles, the particle mass flow rate G_p can be calculated as follows:

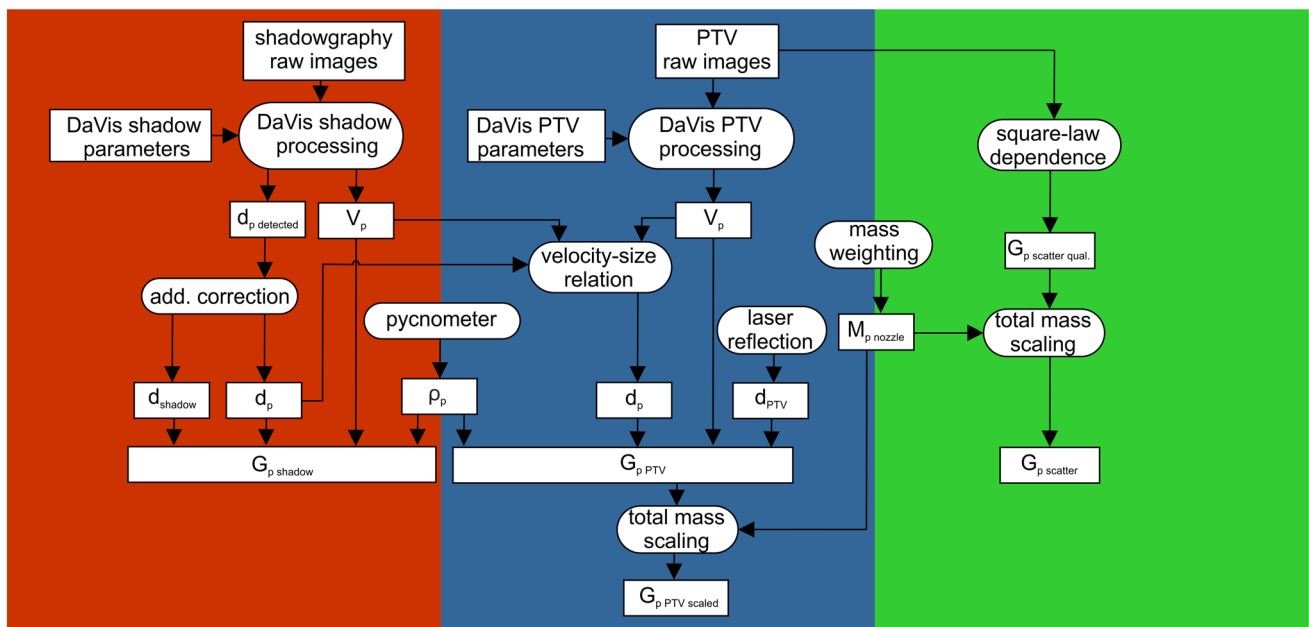


Fig. 5 Sketch of shadowgraphy (red), PTV (blue), and scattered light intensity (green) measurement procedures for G_p determination

$$G_p(t, X, Y) = \frac{4}{3} * \pi * \frac{\rho_p}{L_x * L_y} * \sum_{i=1}^{n_p(t, X, Y)} \frac{\left(\frac{d_{pi}}{2}\right)^3 * V_{p_i}}{d_i},$$

$$[G_p] = \frac{kg}{m^2s} \tag{1}$$

The volume-of-interest (VOI) has the dimensions Ly and Lx with the thickness d. It is located at the position X and Y. All particles, which are located in VOI at time t, are summarized with $n_p(t, X, Y)$. Because the shadowgraphy’s measurement volume thickness d_{shadow} is a function of the particle diameter d_p (see Fig. 10), it must be placed within the sigma sign in Eq. (1). PTV’s measurement volume thickness d_{PTV} only depends on Y. The parameter V_p is the magnitude of the particle velocity. In the following, the spatially resolved G_p distribution across the nozzle exit is named G_p profile.

For a better understanding of several following analyses and subsections, an overview of the three separate measurement approaches, based on shadowgraphy (red), PTV (blue), and scattered light intensity (green), is sketched in Fig. 5. The processing steps are explained in detail in the respective subsections.

2.6 Total particle mass and scaling

The total particle mass passing the nozzle $M_{p\ nozzle}$ is defined as follows:

$$M_{p\ nozzle} = \Delta M_{\text{seeding device}} - M_{p\ collected} \tag{2}$$

The parameter $\Delta M_{\text{seeding device}}$ is the mass difference of the seeding device before and after each run. The seeding device mass was determined with a Kern DS60K0.2 balance. The total particle mass, collected with the injection collection probe, is expressed by $M_{p\ collected}$. It was measured with a Kern PCB 1000–2 balance. The uncertainty of $M_{p\ collected}$ was assumed to be 0.05 g, while the uncertainty of the $\Delta M_{\text{seeding device}}$ measurement was the spread of weighting the seeding device three times. It was assumed that no particles deposited within the facility.

In runs in which the aerosol spectrometer was installed at the injection collection probe, no information regarding the difference between $M_{p\ nozzle}$ and $\Delta M_{\text{seeding device}}$ was achieved. To fill this lack of information, a general relation between $\Delta M_{\text{seeding device}}$ and $M_{p\ collected}$ was built and $M_{p\ collected}$ was interpolated. That general relation was taken from runs in which the collection probe was installed.

While G_p is a spatially and temporally resolved value, $M_{p\ nozzle}$ is an integral value. By assuming a semi-axisymmetric G_p distribution, the calculated total particle mass $M_{p\ calc}$ can be defined as follows:

$$M_{p\ calc} = \pi * \int_0^{t_{meas}} \int_{\frac{-d_{nozzle}}{2}}^{\frac{d_{nozzle}}{2}} G_p(t, y) * |y| * dy * dt \tag{3}$$

Considering the time-averaged $\overline{G_p}$, Eq. (3) is reduced to:

$$M_{p\ calc} = \pi * t_{meas} * \int_{\frac{-d_{nozzle}}{2}}^{\frac{d_{nozzle}}{2}} \overline{G_p}(y) * |y| * dy \tag{4}$$

The parameter d_{nozzle} is the nozzle exit diameter. In the above-mentioned equations, t_{meas} is the evaluation time of shadowgraphy and PTV, given in Table 2 for each run. This time is the period in which all particles were assumed to pass the nozzle. To confirm this assumption, a time-resolved Palas aerosol spectrometer was installed (see Sect. 2.1).

In the PTV and scattered light intensity processing, the G_p values were scaled to fit to $M_{p\ nozzle}$:

$$M_{p\ nozzle} = \pi * t_{meas} * \int_{\frac{-d_{nozzle}}{2}}^{\frac{d_{nozzle}}{2}} \overline{G_{p\ scaled}}(y) * |y| * dy \tag{5}$$

For scaling, the following formulation was used:

$$\overline{G_{p\ scaled}}(y) = \frac{M_{p\ nozzle}}{M_{p\ calc}} * \overline{G_p}(y) \tag{6}$$

2.7 Pycnometer measurements

To have reliable values for the particle density (ρ_p), the investigated particle materials, namely Al_2O_3 , MgO , and SiO_2 , were analyzed with a 100-ml large pycnometer. A sartorius ED6202s scale with a maximum capacity of 6200 g and a display accuracy of 0.01 g was used for scaling. The pycnometer was filled with distilled water at approx. 290 K. The assumed water density was $998.8\ kg/m^3$. The particle density of MgO was additionally measured with the help

Table 3 Final detection parameters of LaVision DaVis ParticleMaster shadowgraphy

Parameter name	Unit	Nominal value
Normalization radius	px	10
Pixel noise reduction	–	‘WEAK’
Binarization threshold	%	13
Minimum shadow area	px	3
Minimum (gradient) slope	%	3
Dark level	Count	0
Maximum size deviation	%	50
Particle displacement range in x-direction	px	40 ± 60
Particle displacement range in y-direction	px	0 ± 5

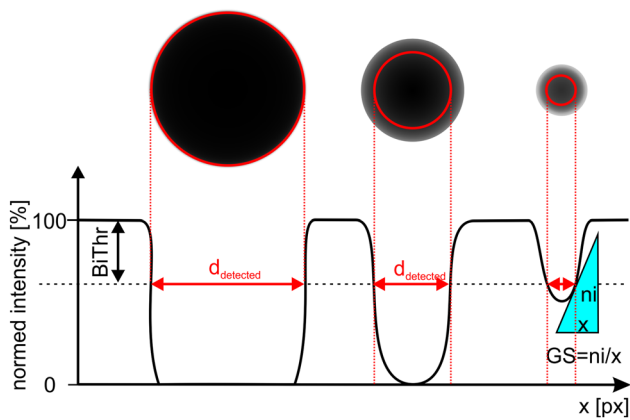


Fig. 6 Gray levels of differently sized shadows, adapted from (Koh et al. 2001). Graphical definitions of BiThr and GS are included

of paraffin oil, having a density of 845.9 kg/m^3 . This was done to exclude any reaction processes of MgO and H_2O to magnesium hydroxide, $\text{Mg}(\text{OH})_2$. To avoid any air bubbles within the pycnometer, the particle material and the liquid were shaken until no air bubbles were visible any more. Each material density was measured three times with water.

2.8 Shadowgraphy approach

Direct imaging of particles is a straightforward technique for determining velocity and size even from irregular-shaped particles. Multiple names were used for this technique in the past: shadowgraphy technique (Castanet et al. 2013, Dehnadfar et al. 2012, Legrand, Nogueira, Lecuona and Hernando 2016, Wang et al. 2017), particle droplet image analysis (PDIA) (Anand et al. 2012; Castanet et al. 2013; Ju et al. 2012; Kashdan et al. 2003; Senthilkumar et al. 2020), backlight photography (Zhou et al. 2020), image processing technique (Koh et al. 2001; Lee and Kim 2004), image-based drop-sizing techniques (Fdida and Blaisot 2009), shadow imaging (Putkiranta et al. 2008), or just imaging (Kim and Kim 1994). In the following, the term shadowgraphy is used. An overview of several shadowgraphy studies and their important investigation parameters is given in Table 9. Advantages of shadowgraphy are: an economical setup, robustness, simple optical alignment, large dynamic range, and its ability to measure non-spherical particles. Furthermore, it is also capable to visualize shocks in supersonic flows. Its disadvantages are: strong dependencies on the chosen image processing algorithm, especially the ambiguity of defining the perimeter of unfocused particles, and the consideration of different measurement volume thicknesses, the so-called depth-of-field (DOF), for different particle sizes. These aspects are the two major error sources by using shadowgraphy (Chigier 1991).

Shadowgraphy measures the intensity decrease on a bright illuminated background, caused by particle shadows. The general intensity distribution of a particle shadow depends on its size and the defocus level (Koh et al. 2001). In the framework of the implemented shadowgraphy image processing in this study, particles were detected by means of the LaVision ‘DaVis ParticleMaster Shadowgraphy’ software. This code follows the processing steps of image normalization, denoising, binarization, and filtering. Normalization is done with the help of the so-called normalization radius (NorRad), which is the size of a strict-sliding maximum filter. The larger NorRad, the stronger image intensity smoothing effects. Noise reduction can be set with three pre-defined levels ‘weak’, ‘medium’, and ‘strong.’ The binarization threshold level (BiThr) divides the normed image into black and white areas. An overview of all DaVis V10.1 particle detection parameters can be found in Table 3.

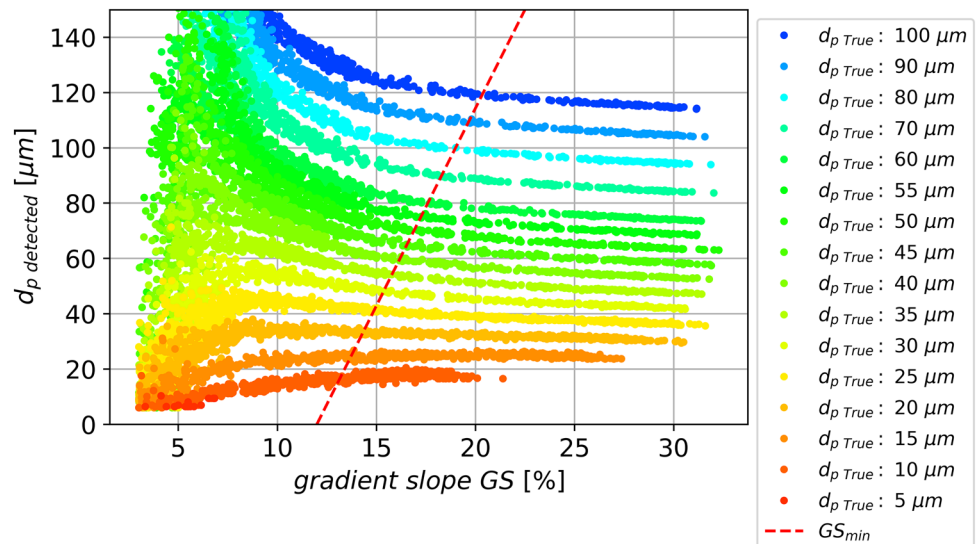
General gray-level distributions for differently sized particle shadows and the definition of BiThr are sketched in Fig. 6. As depicted here and discussed in (Kapulla et al. 2008) for DaVis, the BiThr has a significant influence on the detected particle size ($d_{p \text{ detected}}$). While only large and focused particles are detected with high BiThr values, low values allow detecting also smaller particles, whereby also background noise might be recognized as ghost particles. The default value of BiThr is 50%, given by LaVision (LaVision GmbH 2019a, b).

To measure particles down to 5 to 10 μm in size with the presented optical setup, low binarization thresholds were required, which were significantly lower than the LaVision default value. Furthermore, the minimum detectable shadow area had to be set to 3 px. LaVision states a meaningful minimum value of the minimum detectable shadow area to be 10 px. For lower values, a significant reduction of particle diameter measurement precision has to be expected. To circumvent this, an additional size correction was established. This additional correction had the purpose to cancel out the effect of any particle detection parameter, especially of BiThr, or the NorRad on the particle size measurement. As a consequence, the parameter BiThr could be used to control the minimum detectable particle size if applying the additional size correction, while its effect on the final particle size was eliminated.

Following (Koh et al. 2001), the additional size correction depended on the measured particle size and the defocus level. It is common to use the intensity gradient at the detected particle boundary as defocus parameter, which is called gradient slope (GS) in the following. This parameter was already provided in the DaVis software results. Its definition is illustrated in Fig. 6.

In this study, a depth-of-field calibration was performed with a customized calibration glass target, containing black dots in the range of 3 to 100 μm , mostly in steps of 5 μm .

Fig. 7 Relation between detected size, true size, and gradient slope GS



The target was moved from -3 mm to 3 mm on the z-axis through the focus plane in 0.1 -mm steps. Images were pre-processed, so that dirt on the target and the lenses was digitally removed. With the help of these calibration data, an additional size correction procedure was developed and the shadowgraphy measurement volume thickness was defined. It was assumed that the appearance of calibration dots behaves similar to the appearance of particle shadows in a supersonic flow.

With the help of this calibration, the relation between detected and uncorrected size $d_{p \text{ detected}}$, GS, and true size of the calibration dots ($d_{p \text{ True}}$) was found, which is depicted in Fig. 7. This relation differed between dots, which were placed in front of the focus plane, and dots, which were placed behind the focus plane: For small GS values, the relation for a single dot size was not distinct. Therefore, a minimum GS limit was defined to account only unambiguous data at higher GS values and is marked as dashed red line. Its crossing at $d_{p \text{ detected}} = 0 \mu\text{m}$ is called ‘minimum GS offset’ in the following. The minimum GS limit depended on the relation between $d_{p \text{ detected}}$, $d_{p \text{ True}}$, and GS, which again depends on the optical setup and DaVis particle detection parameters. Similar to (Allofs, Neeb and Gülhan 2022), correction polynomials were defined, allowing to achieve the true size of dots, based on its detected size and GS value:

$$d_{p \text{ True}} = f(d_{p \text{ detected}}, GS) \tag{7}$$

Table 4 Overview of applied filters on shadowgraphy data

Parameter	Unit	Filter
V_x	m/s	300–theoretical velocity
V_y	m/s	–20–20
GS	%	minimum GS offset -

The application of the correction polynomial is called additional size correction in the following. It is assumed that its uncertainty is $1.25 \mu\text{m}$ for each particle.

The measurement volume thickness ($d_{\text{shadow minGS}}$) was defined as the focus depth, in which particle/dot sizes could be properly detected and corrected with the help of the described additional size correction. Depending on the implemented optics, it can be described as a function of particle/dot diameter. Following the remark made in (Legrand, Nogueira, Lecuona and Hernando 2016, Senthilkumar et al. 2020), it is necessary to control if all dots within a defined measurement volume thickness are detected. To check whether this was the case for $d_{\text{shadow minGS}}$, the number of detected dots was counted for each z-position. The number of detected dots was scaled by its maximum and is called count efficiency (CE) in the following. If CE is 1 in the entire $d_{\text{shadow minGS}}$, it can be used as final shadowgraphy measurement volume thickness d_{shadow} .

The minimum detectable size of shadowgraphy ($d_{p \text{ min}}$) is defined as the particle size which can barely be detected, while the minimum size at which all dots can be detected is named $d_{p \text{ min, full}}$.

Finally, it must be noted that the additional size correction and the d_{shadow} determination were done individually for each camera and for $1 \times 1.2 \text{ mm}^2$ sections of the shadowgraphy images.

The shadow velocity was determined with the help of cross-correlation: Two illumination pulses with the predefined Δt were used to generate two shadow images. The shadow displacement on these two images was measured. The ratio between displacement and time separation is the shadow velocity. The uncertainty in shadowgraphy velocity measurement was assumed to be 0.2 px , the same value as reported in (Allofs, Neeb and Gülhan 2022). Additional filters were applied on the corrected shadowgraphy data,

which are listed in Table 4. The theoretical velocity is the gas velocity at the nozzle exit, assuming one-dimensional isentropic gas dynamics.

2.9 PTV approach

PTV images were processed with the help of DaVis Flow-Master software. A ‘subtract-over-time’ filter was applied for preprocessing, subtracting the time-average image from all other images. The vector processing was split into two steps: First, regular PIV vector fields were achieved. Here, a multi-pass vector calculation with an initial interrogation window size of $96 \times 96 \text{ px}^2$ and a final interrogation window size of $24 \times 24 \text{ px}^2$ was used. The overlap was set to 50%. In a second step, PTV vector data were calculated, based on the PIV vector fields. The allowed particle size range was between 2 and 500 px, and the correlation window size was set to 32 px. A variation in correlation window size resulted in negligible differences of the PTV data. PTV velocity uncertainty was calculated in the same manner as described in (Allofs, Neeb and Gülhan 2022): PIV velocity uncertainty was achieved with the correlation statistics method, implemented in the DaVis software. With the help of a customized mapping function, the PIV velocity uncertainty was interpolated onto the PTV velocity data.

To achieve particle mass flow rates from PTV velocity data, the size of the particles and the size of the measurement volume had to be estimated. Due to their large inertia and the small size of the nozzle, the investigated particles achieved lower velocities than the gas velocity, depending on their size (Allofs, Neeb and Gülhan 2022). Thus, a functional relation between d_p and V_p was defined, depending on flow conditions and the particle material. This relation is called particle velocity-size relation, is based on the shadowgraphy data, and is only applicable to the investigated flow setup. Assuming the validity of the velocity-size relation over the entire nozzle exit, PTV velocity data can be converted into size data:

$$d_{p \text{ PTV}} = f(V_{p \text{ PTV}}) \tag{8}$$

The PTV measurement volume thickness (z_{PTV}) was assumed to be the light sheet thickness, since this was much smaller than the DOF of the PTV camera C3. In contrast to shadowgraphy, the z_{PTV} only depends on the y-position.

Following the suggestion made in (Allofs, Neeb and Gülhan 2022), a new approach was tested to measure the light sheet thickness accurately. A tilted calibration plate was moved through the focus plane, while the laser was switched on the lowest power level and the flow was turned off. Recordings were made with the C3 camera. The width of the laser reflections at different y-positions was measured, which was converted into the laser sheet thickness. This was done for the ‘Master’ (first) and ‘Slave’ (second) laser pulse.

The uncertainty of the measurement volume thickness estimation was assumed to be 3 px, which were approx. $75 \mu\text{m}$.

Several filters were applied onto the PTV data. These are listed in Table 5.

All these filters were used to exclude false vectors. The limitation of the correlation value is a recommendation given in (Lavisio GmbH 2019a, b).

The resulting particle mass flow rate, based on PTV data, is named $G_{p \text{ PTV}}$. Based on the scaling formulation given in Eq. (6), the scaled particle mass flow rate ($G_{p \text{ PTV scaled}}$) was also calculated.

2.10 Scattered light intensity approach

Another approach for determining the spatially resolved particle mass flow rate profile used scattered light intensity profiles across the nozzle exit. This method was presented in (Vasilevskii and Osipov 1999) and was also included in (Allofs, Neeb and Gülhan 2022). Following the square-law dependence between scattered light of particles and their diameter (Hovenac 1987) and Eq. (1), it was assumed that the following relationship between scattered light intensity and the qualitative particle mass flow rate ($G_{p \text{ scatter qual.}}$) is valid:

$$\text{scattered light intensity}^{1.5} \sim d_p^3 \sim G_{p \text{ scatter qual.}} \tag{9}$$

The scattered light signal was taken from the PTV camera C3. Only images were considered, which were recorded during the measurement time t_{meas} . Afterward, the average from all of these images was subtracted from every image. The subtracted images were summed up, and the mean intensity for every y-position was built. Considering $G_{p \text{ scatter qual.}}$ and the scaling formulation given in Eq. (6), the particle mass flow rate profile, based on scattered light intensity ($G_{p \text{ scatter}}$), was calculated.

3 Results

The results section is organized as follows: In the beginning, results of required sub-analyses, namely total particle mass, particle density, and measurement volume thickness analyses, are reported. Following the guideline of this work, particle size distributions of shadowgraphy and PTV are qualitatively compared to reference data. Then, particle mass

Table 5 Overview of applied PTV data filters

Parameter	Unit	Filter
V_x	m/s	300–theoretical velocity
V_y	m/s	–20–20
d_p	μm	0–60
correlation value	–	0.6–0.7

flow rate uncertainty calculations are presented. In the end, particle mass flow rates for all investigated flow conditions and particle materials are compared.

3.1 Total particle mass

The relation between collected particle mass $M_{p, \text{collected}}$ and mass differences of the seeding device $\Delta M_{\text{seeding device}}$ is illustrated in Fig. 8. The collected particle mass is around 1/44 of the total particle mass loss of the seeding device. This relation is independent of particle material. Since in some tests the aerosol spectrometer was installed, $M_{p, \text{collected}}$ could not be determined. For the following analyses, $M_{p, \text{nozzle}}$ was assumed to be for the tests with implemented aerosol spectrometer:

$$M_{p, \text{nozzle}} = \Delta M_{\text{seeding device}} * (1 - 1/44) \tag{10}$$

In runs in which the aerosol spectrometer was installed, no unintended seeding was observed. The authors assumed that this was also the case for all other runs. As a consequence, all particles passed the nozzle in t_{meas} and so, Eq. (3) and Eq. (4) can be used for the following scaling.

3.2 Particle density

The pycnometer measurement results are summarized in Table 6. The reference particle density for Al_2O_3 , MgO , and SiO_2 was taken from (Molleson and Stasenko 2017) and (Vasilevskii and Osipsov 1999), (Niosh Pocket Guide to Chemical Hazards —Magnesium Oxide Fume 2022), and (Palmer et al. 2020), respectively. The difference between reference value and the mean value of the three pycnometer measurements is also given.

For the following analyses, the mean measured values are taken for particle mass flow rate calculations. A particle density uncertainty of 38 kg/m^3 , 77 kg/m^3 , and 6 kg/m^3 for Al_2O_3 , MgO , and SiO_2 particles is assumed, respectively. These uncertainties correspond to the largest difference between measured and mean densities.

3.3 Measurement volume thicknesses

As mentioned in Sect. 2.8, the final measurement volume thickness d is defined as the minimum volume thickness, which is limited by the minimum GS and in which the count efficiency CE is 1. The count efficiency for the investigated z-positions and the final shadowgraphy detection parameters (see Table 3) are plotted in Fig. 9. With the selected settings, 5- μm -large calibration dots were barely detected in the focus plane ($z=0 \text{ mm}$). This size is defined as the minimum

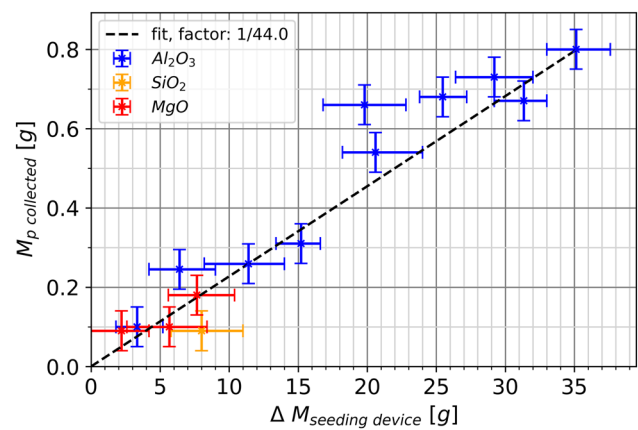


Fig. 8 Relation between total particle mass loss in the seeding device and the particle mass, collected with the injection collection probe

detectable size $d_{p, \text{min}}$. The minimum size at which all dots can be detected $d_{p, \text{min, full}}$ is $10 \mu\text{m}$. For some z-positions and calibration dot sizes, CE is larger than 1. The authors observed that this is an effect of particle detection at low BiThr values: Unfocussed shadows were split into multiple shadows, resulting in CE larger than 1. To exclude this split effect, the z-range was defined as $d_{\text{shadow CE}=1}$ in which CE is always 1. Different shadowgraphy measurement volume thicknesses for individual dot sizes are plotted in Fig. 10. For all calibration dot sizes, $d_{\text{shadow CE}=1}$ is larger than $d_{\text{shadow minGS}}$. This means that the count efficiency is always sufficiently high in $d_{\text{shadow minGS}}$, which is used as final shadowgraphy measurement volume thickness d_{shadow} in the following.

The measured laser sheet thickness, which can be used for d_{PTV} , is plotted in Fig. 11 for both laser pulses, namely ‘Master’ and ‘Slave.’ The sheet thickness increased from top to bottom, from approx. 0.25 mm to approx. 0.5 mm. The mean of both laser pulses is marked with a red dashed line. It was assumed that all particles were detected by PTV within its measurement volume.

Table 6 Pycnometer measurement results

Parameter	Unit	Al_2O_3	MgO	SiO_2
Measured ρ_p , run 1, H_2O	kg/m^3	3846	3165	2630
Measured ρ_p , run 2, H_2O	kg/m^3	3907	3056	2640
Measured ρ_p , run 3, H_2O	kg/m^3	3901	3182	2638
Measured ρ_p , run 4, paraffin oil	kg/m^3	—	3091	—
Measured ρ_p , run 5, paraffin oil	kg/m^3	—	3174	—
Measured ρ_p , mean	kg/m^3	3884	3133	2636
Reference ρ_p	kg/m^3	3950	3580	2650
Difference	%	−1.7	−12.5	−0.5

3.4 Particle size distributions

The measured particle size distributions were compared to reference measurements, which were conducted independently of the GBK facility or flow conditions. These reference data were achieved with a dynamic image analysis device ‘PartAn SI’ of Microtrac.

Regarding the reference flow condition, the Al_2O_3 size distribution of test run A-23-2 is shown in Fig. 12, while the MgO size distribution of test run M-23-1 is illustrated in Fig. 13. Although there is no reference size distribution of SiO_2 particles available, the shadowgraphy and PTV size distributions of test run S-23-1 are given in Fig. 14. The size bins correspond to shadowgraphy defined size bins with a bin width of $2.5 \mu m$. The variable measurement volume thickness of shadowgraphy data was considered in the following plots, indicated with the addition ‘DOF corr.’

3.5 Particle mass flow rate uncertainty

In general, linear error propagation theory was implemented to determine uncertainties. In terms of the shadowgraphy and PTV approach, particle mass flow rate was calculated with Eq. (1). Hence, particle mass flow rate uncertainty depended on the uncertainties of particle number, velocity, size, density, and the size of the measurement volume. Considering the scattered light intensity approach, it was assumed that particle mass flow rate uncertainty only depends on $M_{p, nozzle}$ uncertainty. This was also the case for $G_{p, PTV, scaled}$.

It was also checked how the resulting shadowgraphy G_p is affected by single DaVis shadowgraphy detection parameters, namely BiThr and NorRad. Therefore, a parameter variation of BiThr and NorRad was performed. As explained

in Sect. 2.8, the minimum GS offset had to be adapted to account for a measurement volume thickness in which CE is 1.

In the following, shadowgraphy data from the test run A-32-2 (see Table 2) were taken to determine the G_p uncertainty of the presented shadowgraphy approach, including the additional size correction and the d_{shadow} determination. The parameter setting as well as the resulting mean G_p value and its uncertainty are given in Table 7. While an increase of NorRad results in an decreased G_p , G_p increases if BiThr and minimum GS offset are also increased.

The average of all G_p mean values is approx. $6.1 \text{ kg/m}^2\text{s}$, close to the result with the setting NorRad = 10 px and BiThr = 13%. The G_p uncertainty for each parameter setting is approx. $0.04 \text{ kg/m}^2\text{s}$, namely up to 1%. The maximum difference between G_p mean values from their average value

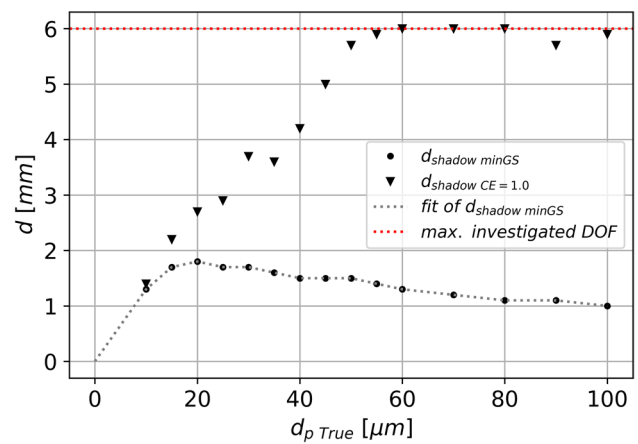
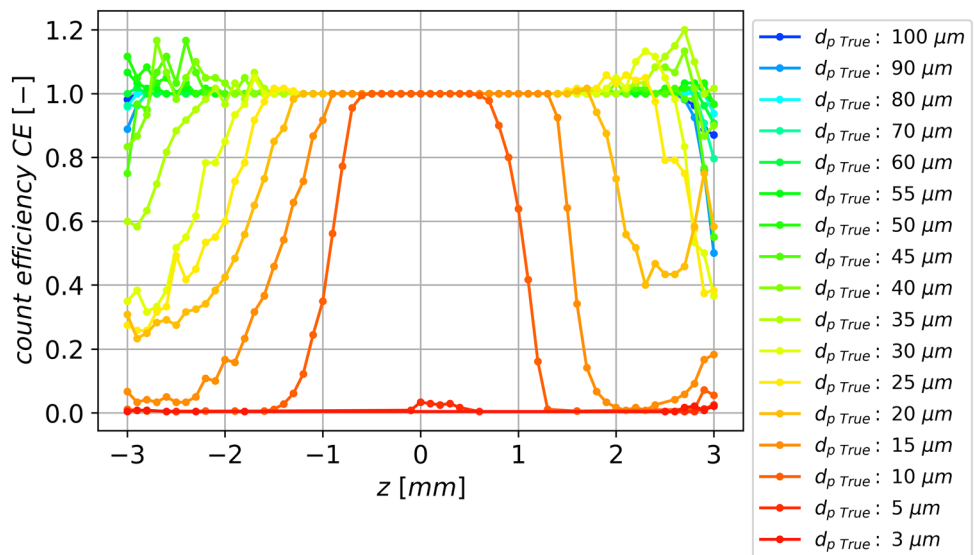


Fig. 10 Relation between $d_{shadow \text{ minGS}}$ and $d_{shadow \text{ CE}=1}$, depending on calibration dot size. CE is always 1 for $d_{shadow \text{ minGS}}$

Fig. 9 Count efficiency vs. z-position, BiThr = 13%, and NorRad = 10 px, C1



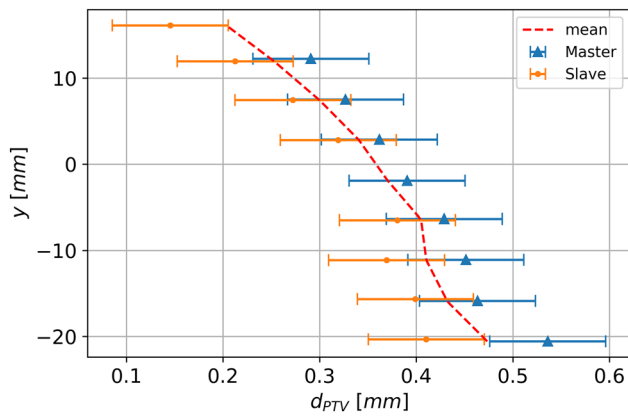


Fig. 11 PTV light sheet thickness for both laser pulses at different y-positions

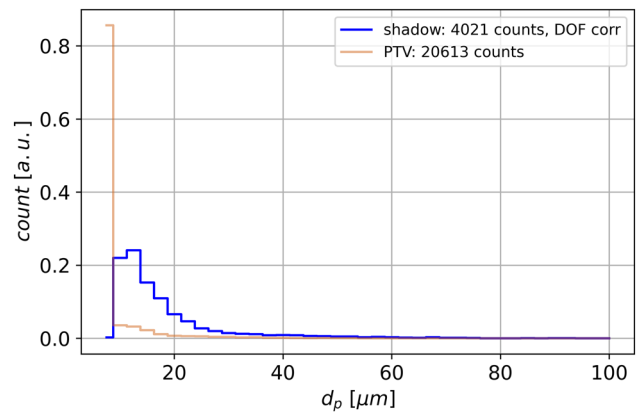


Fig. 14 Particle size distribution, SiO₂, run S-32-1

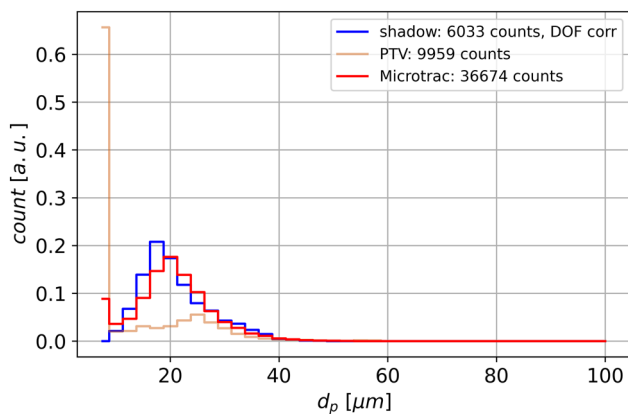


Fig. 12 Particle size distribution, Al₂O₃, run A-32-2

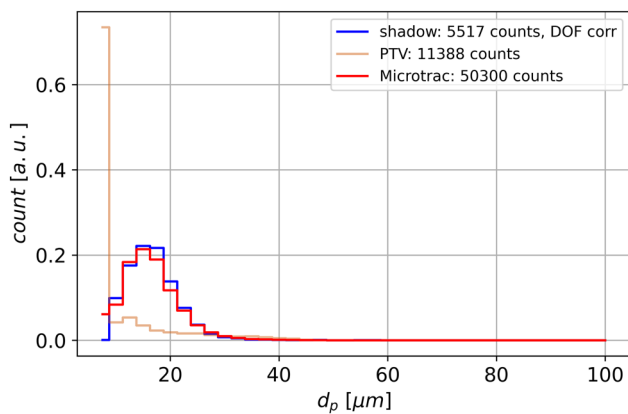


Fig. 13 Particle size distribution, MgO, run M-32-1

is approx. 30%. The percentage of particles smaller than $d_{p \text{ min, full}} = 10 \mu\text{m}$, which are the ‘invisible’ particles for shadowgraphy, on the total G_p is less than 2% for Al₂O₃ particles. Since the variation of G_p mean values is significantly

larger than the respective G_p uncertainties, an overall uncertainty of 30% for shadowgraphy’s G_p determination of all tests was assumed in the following. The parameter setting containing $\text{NorRad} = 10 \text{ px}$ and $\text{BiThr} = 13\%$ was chosen for the following analysis.

The particle mass flow rate uncertainties of the three measurement approaches are summarized in Table 8. While shadowgraphy’s uncertainty was set to 30%, the uncertainty of $G_{p \text{ PTV}}$, $G_{p \text{ scattered}}$, and $G_{p \text{ PTV scaled}}$ varied for each test run. As a consequence, not only the mean, but also the corresponding interquartile ranges IQR of the respective particle mass flow rate uncertainties are listed.

3.6 Particle mass flow rate profiles

In this section, the particle mass flow rate profiles of the three measurement approaches are compared for each particle material and for the reference flow condition. These profiles are illustrated in Figs. 15, 16, and 17 for Al₂O₃, MgO, and SiO₂ particles, respectively. Solid, dotted, and dash-dotted lines are representing the mean G_p values, while the transparent areas illustrate the respective measurement uncertainty. Shadowgraphy results are colored red, PTV data are colored blue, scaled PTV data are colored golden, and scattered light intensity data are colored green.

To compare the three measurement approaches for all investigated flow conditions and particle materials, the particle mass flow rates only in the y-range between -2.4 and 2.4 mm were considered and averaged. The particle mass flow rates of shadowgraphy, PTV, and scaled PTV were quantitatively compared to the particle mass flow rate of the scattered intensity approach. The comparisons are illustrated in Figs. 18, 19, and 20. The colors represent the selected particle material. Linear fits were calculated and plotted as dashed lines for the visualization of a general behavior between the respective measurement approaches. A unity

Table 7 Parameter variation effects on shadowgraphy's G_p . The parameter variation has more influence on G_p than the estimated uncertainty based on individual particle parameter uncertainties

NorRad [px]	BiThr [%]	min. GS offset [%]	G_p [kg/m ² s]
10	13	12	6.19 ± 0.04
5	13	12	6.89 ± 0.04
15	13	12	5.69 ± 0.04
25	13	12	5.21 ± 0.03
10	10	12	4.28 ± 0.03
10	20	14	7.24 ± 0.05
10	30	20	7.02 ± 0.04

Table 8 Relative particle mass flow rate uncertainties of all measurement approaches

Parameter	Unit	Mean (IQR) uncertainty
G_p shadow	%	30
G_p PTV	%	76 (40–100)
G_p scattered / G_p PTV scaled	%	28 (11–37)

line with unitary angular coefficient is also shown for better orientation.

4 Discussion

This study focusses on three different non-intrusive approaches for the determination of particle mass flow rate G_p . These approaches are based on shadowgraphy, PTV, and scattered light intensity, respectively. After a general discussion of these three methods, the focus moves to the particle size distribution and particle mass flow rate results.

From the literature, shadowgraphy is mostly used for particle size distribution analysis and only rarely implemented for particle mass flow rate or particle concentration determination (Hufnagel et al. 2018; Lecuona et al. 2000), see Table 9). Rather, it is mainly used for the investigation of drops and not irregular particles. Compared to the procedure given in (Allofs, Neeb and Gülhan 2022), the optical resolution was increased from 211 to 327 px/mm. The increase of optical resolution reduced the amount of invisible particles, smaller than the minimum detectable particle size of shadowgraphy, from 17% to less than 2%. These particles were stated to be the main driver for particle mass flow rate uncertainty in (Allofs, Neeb and Gülhan 2022). Compared to

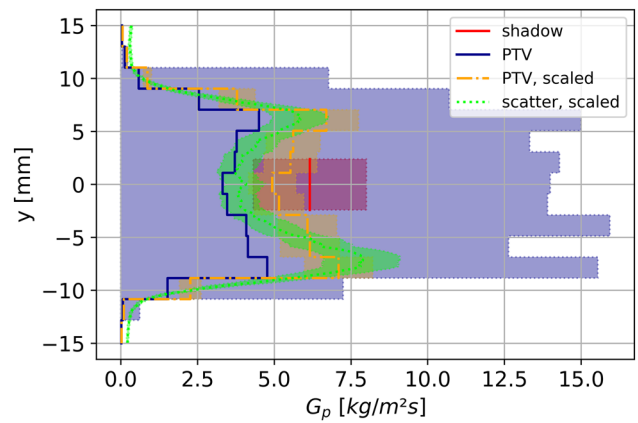


Fig. 15 Particle mass flow rate profiles, run A-32-2, $p_0=0.952$ MPa, $T_0=374.5$ K, Al_2O_3

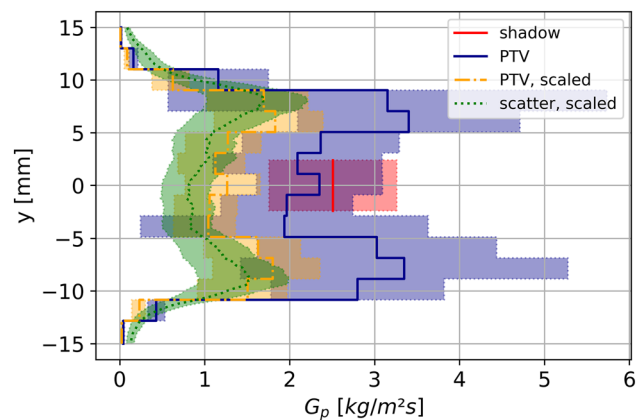


Fig. 16 Particle mass flow rate profiles, run M-32-1, $p_0=0.950$ MPa, $T_0=373.5$ K, MgO

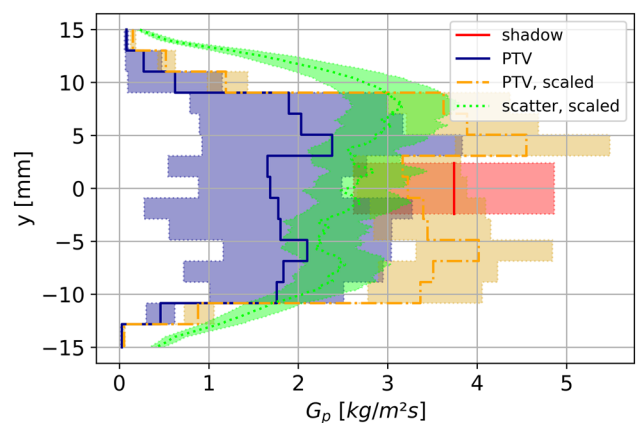


Fig. 17 Particle mass flow rate profiles, run S-32-1, $p_0=0.952$ MPa, $T_0=374.0$ K, SiO_2

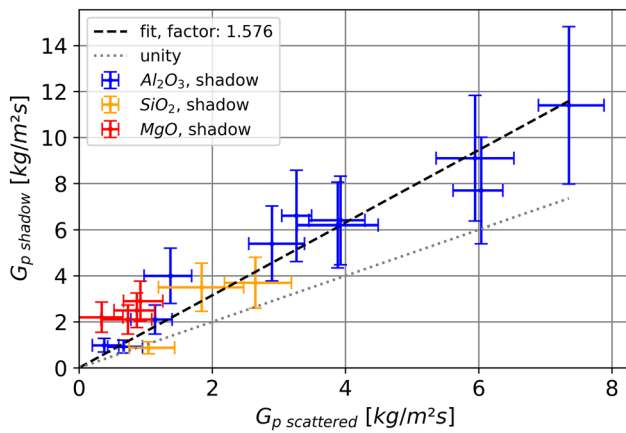


Fig. 18 Comparison of G_p in the range of -2.4 to 2.4 mm, measured with the scattered light intensity approach and shadowgraphy

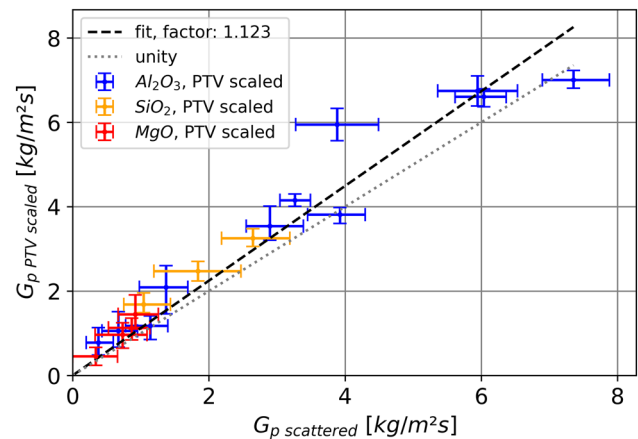


Fig. 20 Comparison of G_p in the range of -2.4 to 2.4 mm, measured with the scattered light intensity approach and the scaled PTV approach

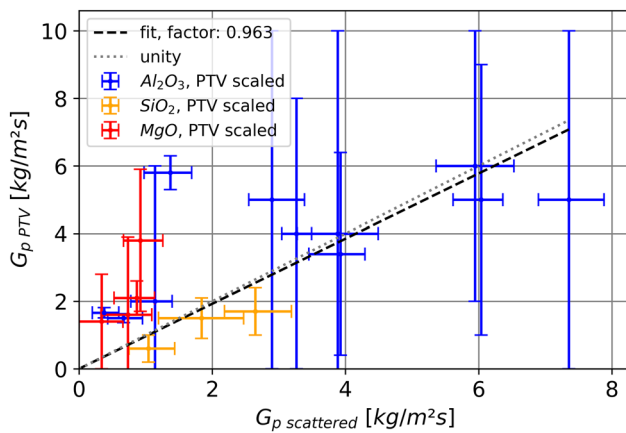


Fig. 19 Comparison of G_p in the range of -2.4 to 2.4 mm, measured with the scattered light intensity approach and the PTV approach

other shadowgraphy-related studies summarized in Table 9, the presented optical resolution is in an upper medium range.

This study contains a parameter variation of DaVis shadowgraphy particle detection settings which was not performed in terms of particle mass flow rate uncertainty determination in any other study so far, to the best knowledge of the authors. This variation led to a spread of particle mass flow rates up to 30% when applying several additional correction procedures. This value is significantly larger than the predicted uncertainty values based on linear error propagation theory. It was found that an increase of the normalization radius $NorRad$ resulted in a decrease of G_p , while an increase of G_p was observed when increasing $BiThr$ and increasing the minimum GS offset. The latter was required for the distinct determination of the particle size correction polynomials.

A control of the count efficiency of the presented shadowgraphy procedure indicated that the measurement volume thickness $d_{shadow, CE=1}$, in which all calibration dots were detected, was larger than the measurement volume thickness limited by the minimum GS limitation $d_{shadow, minGS}$. The relation between $d_{shadow, CE=1}$ and the calibration dot size can be approximated with a linear relation, as it is common in previous studies (see Table 9). In contrast, the relation between calibration dot size and $d_{shadow, minGS}$ is more complex. Since $d_{shadow, CE=1}$ is larger than $d_{shadow, minGS}$, it is assumed that all particles were detected in the selected measurement volume. This is valid as long as shadows of particles in supersonic flows behave similar to circular dots on a glass-target. A comparison between bubble-based and glass target-based calibrations was made in (Senthilkumar et al. 2020), showing differences in the detected measurement volume thickness. In future studies, it has to be checked whether shadowgraphy’s measurement volume thickness, measured by means of a glass target without flow, can be applied to the supersonic flow environment.

In general, comparing different shadowgraphy image processings from the literature is a complex task. The relation between shadow appearance and defocus level strongly depends on the selected optical arrangement. Even if all shadowgraphy processing algorithms are publicly available, the application of just one approach on a raw shadowgraphy data set is elaborate. Sharing shadowgraphy raw data is difficult due to its large data file sizes. Due to different calculation methods, a comparison of the found shadowgraphy’s G_p uncertainty cannot be made. An advantage of the presented shadowgraphy procedure is the fact that it is based on the commercially available LaVision DaVis software. This can simplify

the implementation of the shadowgraphy approach and the additional size correction to other researchers who have already used DaVis (e.g., Anand et al. 2012; Ghaemi et al. 2010, Hufnagel, Werner-Spatz, Koch and Staudacher 2018).

PTV was used to detect individual particle velocities across the nozzle exit diameter. To achieve particle mass flow rates from PTV data, several additional measurements had to be taken, which made the PTV procedure quite complex and elaborate (see Fig. 5). In particular, the data conversion from velocity into size data had to be adapted for each flow condition. In general, this conversion is only applicable to setups, in which a monotonous particle velocity-size relation can be found. The measurement of the light sheet thickness indicated that the laser was not focused exactly on the flow axis, but on the top edge of the nozzle.

The scattered light intensity approach is the simplest of the presented approaches. Similar to PTV, it required also the PTV raw images and the total mass scaling. In contrast to the work of (Vasilevskii and Osiptsov 1999), in this study the scattered light intensities were raised by the power of 1.5 to fit the square-law dependence between scattered light and particle diameter (Hovenac 1987), which seems to be more reasonable. PTV and scattered light profiles were scaled to fit the total particle mass whose uncertainty dominates the respective particle mass flow rate uncertainty. The total particle mass uncertainty was caused by the large ratio between balance uncertainty and the small weight of seeded particles. The balance uncertainty can only be reduced by using a different balance. An idea was to predict $M_{p, \text{nozzle}}$ by only considering $M_{p, \text{collected}}$. Although there is a linear relation between those values, this relation is too noisy for proper prediction. In future, it seems to be advisable to increase the total mass of seeded particles by increasing particle mass flow rate or by increasing measurement time.

The presented shadowgraphy procedure and the additional size correction resulted in a good agreement of particle size distribution of Al_2O_3 and MgO particles, compared to reference measurements by Microtrac. Shadowgraphy detected slightly more Al_2O_3 particles in the range of 15 to 17.5 μm . Because particle agglomeration effects in the reference measurements were minimized, the authors conclude that Al_2O_3 particles and MgO particle did not show significant agglomeration within the GBK flow. The SiO_2 particle size distribution tends to smaller particles than those of MgO and Al_2O_3 . Some SiO_2 particles up to 80 μm were detected. The authors assume that those particles were agglomerated. This agglomeration behavior of SiO_2 particles was also described in (Esser et al. 2006). In future studies,

reference size distribution measurements should clarify if SiO_2 particles were agglomerated.

PTV-based size distributions were in poor agreement with the Microtrac reference size distributions for all of the investigated flow conditions. As expected, most of PTV's detected particles were in the size range of 0 to 7.5 μm . The authors assume that the large velocity uncertainty is responsible for that poor agreement. This uncertainty can be significantly decreased with two strategies: increasing the particle displacement of the PTV recordings, and decreasing saturation effects caused by large particles. The latter was done with the help of a laser light intensity reduction, resulting in moderate success. As a conclusion, increasing the particle displacement from the current value of 5 to 10 px seems to be the best way to decrease PTV uncertainty. Since PTV and shadowgraphy used the same illumination source, a simultaneous measurement could be quite challenging, though.

The pycnometer results indicated that the measured density ρ_p of Al_2O_3 and SiO_2 particles agreed to reference values from literature, while the measured MgO density was 12.5% lower. The authors assume that this significant decrease can be caused, first, by a partial chemical reaction of MgO with humidity, resulting in $\text{Mg}(\text{OH})_2$, whose density is around 2380 kg/m^3 , and second, by contamination during the additional sieving process. A reaction of MgO with water within the pycnometer during the measurement could be excluded, because no difference in MgO density between water-filled pycnometer measurements and paraffin-oil-filled pycnometer measurements was observed. The authors made another pycnometer measurement with smaller-sized MgO particles, which were not additionally sieved. The resulting particle density was even lower than 3133 kg/m^3 , which seems to exclude contamination as the only reason for the low density. As a consequence, careful attention must be given to the reactivity of particle material and its storage in future studies.

While simple dust catcher probes suffered from collecting particles in preliminary tests in the GBK facility, the results of the scaled scattered light intensity approach were used for referencing, since this technique was already used in a similar manner in (Vasilevskii and Osiptsov 1999). An improvement of dust catcher probes for the use in the GBK facility is recommended in future studies, to have integrated reference particle mass flow rates like in (Kudin et al. 2013; Polezhaev et al. 1992).

The PTV approach resulted not only in a poor agreement of the particle size distribution, but also the particle mass flow rates showed large deviations from the scaled scattered light intensity G_p values, preventing useful interpretation of the results. The authors assume that the PTV approach has to be applied on PTV data with a

significant larger particle displacement and reduced saturation effects, to conclude if the PTV approach is generally feasible. The scaling of the PTV profile to the total mass of seeded particles resulted in approx. 12% higher particle mass flow rates, compared to those of the scaled scattered light intensity. Both scaled approaches have a G_p uncertainty of approx. 28% (IQR 11–37%) which is dominated by the uncertainty of $M_{p, \text{nozzle}}$. As expected, the larger the $M_{p, \text{nozzle}}$, the lower its relative uncertainty.

Shadowgraphy's G_p is approx. 58% higher than those of the scaled scattered light intensity. Assuming that the latter one is correct and considering the fact that shadowgraphy measured the particle size distribution and velocity properly, the main driver for the increased G_p could be an underestimated measurement volume thickness d_{shadow} . However, in the study of (Senthilkumar et al. 2020), it is proposed that a DOF calibration with the help of a glass-target tends to an overestimated d_{shadow} .

On the other hand, it is also feasible that shadowgraphy's G_p is correct and that the scaled scattered light intensity approach and the scaled PTV approach are underestimating G_p . This can be true if the assumption of the semi-axisymmetric flow is not appropriate. Taking the single particle injection point within the stagnation chamber into account, particles can accumulate on the x - y plane. This fact would increase shadowgraphy's G_p , but not the G_p values of the scaled scattered light intensity and the scaled PTV data, because these are scaled to the total particle mass. To close this gap of information, it has to be shown in future studies whether the particle mass flow rate distribution is axisymmetric or semi-axisymmetric. In any case, the authors assume that the shadowgraphy's G_p value can be used as an initial guess.

5 Conclusion

To the best knowledge of the authors, this is the first study in which particle mass flow rates were determined quantitatively with the help of simultaneous and individual determination of particle number density, particle size, and velocity in supersonic flows. This work has significantly improved the measurement approaches introduced in (Allofs, Neeb and Gülhan 2022), by the use of a customized calibration target, increased optical resolution, and consideration of the counting efficiency. Multiple supersonic flow conditions and particle materials were tested in the experimental test facility GBK of DLR Cologne.

A qualitative comparison of particle size distributions of Al_2O_3 and MgO particles showed a good agreement of shadowgraphy size data and reference data. SiO_2 particles seemed to agglomerate, which has to be confirmed in future studies.

While pycnometer measurements of Al_2O_3 and SiO_2 particles resulted in particle densities close to reference values, MgO particle density was approx. 12.5% lower. The authors assume that this was caused by a chemical reaction of MgO with humidity to the significant lighter $\text{Mg}(\text{OH})_2$.

A quantitative particle mass flow rate comparison of three non-intrusive measurement approaches was made. A DaVis ParticleMaster software parameter variation was used to determine the particle mass flow rate uncertainty of the presented shadowgraphy approach, which is up to 30%. This value is significantly larger than the predicted uncertainty values based on linear error propagation theory. PTV-based particle mass flow rate is dominated by high uncertainties in the range of 40 to 100%. It is suggested to increase the pixel displacement in PTV's double-images for a significant improvement of PTV's velocity uncertainty. The Particle mass flow rate of the scaled PTV approach is approx. 12% higher than those of the scaled scattered light intensity approach. The particle mass flow rate uncertainty of both is in the range of 11 to 37%. Shadowgraphy detected 58% higher particle mass flow rates in average than the scaled scattered light intensity approach. The latter one assumes a semi-axisymmetric particle mass flow rate distribution across the nozzle exit. Future studies need to investigate the correctness of this assumption, since a particle accumulation along the shadowgraphy measurement plane seems to be possible.

The results of this work are useful to select appropriate measurement procedures for particle mass flow rate determination in future studies. Future work will focus on the correlation between particle mass flow rate and stagnation point heat fluxes, on the improvement of the presented measurement techniques and its applicability to other testing facilities, on the influence of particle shape, and on numerical simulation of particle motion.

Appendix

Overview particle sizing with shadowgraphy

See Table 9.

Table 9 Overview of studies concerning particle sizing by means of shadowgraphy

Authors	Resolution/ magnification	Calibration object, sizes	Focus range, steps	In-focus criterion, based on	d_p -relation	Experimental object/sizes	Parameters (d_p, V_p , mass flow)	Error/uncertainty	Remarks
(Fantini et al. 1990)	12 $\mu\text{m}/\text{px}$, 5.25x	Graticule, black circles, 30–340 μm	± 3 mm, 250 μm steps	Halo-area	Constant, 1 mm	Water spray, 35–125 μm	d_p	–	–
(Kim and Kim 1994)	6.08x, 1.6 $\mu\text{m}/\text{px}$	Reticle, disks 3.9–71.7 μm , glass plate	+ 1 mm, 30 μm	Contrast and gradient	Linear	Fuel injector: 1–40 μm fuel drops	d_p	$d_p < 2.3\%$ for $d_p = 3.9$ μm , else $< 0.7\%$	Additional linear d_p correction
(Lebrun et al. 1996)	3.3x	10–700 μm discs on glass substrate	± 2 mm, 0.1 mm	Contrast	–	–	d_p	$d_p < 10\%$ for 20–160 μm	Two CCDs, power spectrum computation analysis more reliable
(Lecuona et al. 2000)	0.1–0.33x, 125 $\mu\text{m}/\text{px}$ –37 $\mu\text{m}/\text{px}$	Glass spheres 0.3–3 mm	± 100 mm, ~25 mm	Gradient	–	0.5 mm–3 mm	d_p , concentration	d_p : 3–4% for $z = \pm 50$ mm, 2–8% particle concentration, < 12% volume flux number	Overlapping, particle outside focus negligible effect
(Nishino et al. 2000)	6.8 $\mu\text{m}/\text{px}$	Dots on plate, 10–500 μm , ± 1 μm	± 2 mm, 200 μm	Max. gradient	Constant, ± 1 mm	50–200 μm , glass/metal/metal oxide/synthetic particles, spherical/non-spherical	d_p, V_p	$d_p: \pm 4$ μm , for $d_p = 10$ μm : 6%	Stereo system, small dots overestimated, large dots underest., max. vol. fraction 0.1%
(Koh et al. 2001)	2.9x, ~3.1 $\mu\text{m}/\text{px}$	Graticule, dots 2–300 μm	–2.5–1.5 mm, 50–100 μm	$d_p < 30$ μm : contrast, $d_p > 30$ μm : gradient	Linear, two slopes (< 30 μm)	–	d_p, d_{shadow}	$d_p: < 10\%$, $d_{\text{shadow}}: < 10\%$	–
(Kashdan, Shrimpton and Whybrew 2003, Kashdan et al. 2007)	0.7 $\mu\text{m}/\text{px}$	Dots on plate, 18–145 μm , ± 2 μm	± 1.5 mm, 10 μm	70% of max. halo area and gradient	Linear	Spray drops, 10–100 μm	d_p	Statistical uncertainty of cumulative size distribution: 2–3%	Comparison: diode and Nd:YAG illumination: affects d_{shadow} linear d_p correction
(Putkiran, Elooranta, Alahautala and Saarenrinne 2008)	5.43 $\mu\text{m}/\text{px}$	Dots on plate, 3.5–1270 μm	0–1.7 mm, 50 μm	No criteria	Power law, based on particle recognition	$d_p = 79.2$ – 1227 μm	d_p	$d_p = 79.2$ μm : 2.4%, $d_p = 56$ μm : 5%	No out-of-focus d_p correction

Table 9 (continued)

Authors	Resolution/ magnification	Calibration object, sizes	Focus range, steps	In-focus crit- erion, based on	d - d_p -relation	Experimental object/sizes	Parameters (d_p , V_p , mass flow)	Error/ uncertainty	Remarks
(Frida and Blaisot 2009)	14.08 $\mu\text{m}/\text{px}$ / 8.8 $\mu\text{m}/\text{px}$	Calibrated discs: 40 / 150 / 300 μm	± 5 mm, 0.1— 0.5 mm	Contrast, PSF	Constant		d_p	$d_p = 40$ μm , $< 2\%$, general: $< 5\%$	d_{shadow} limited to max d_{shadow} of small- est drop diameter, min $d_p = 20$ μm Application of LaVision ParticleMas- ter, no DOF calibration
(Ghaemi et al. 2010)	0.23 $\mu\text{m}/\text{px}$	—	—	Sharp bounda- ries'	Constant, 0.05 mm	Droplets in effe- rescent spray, 5–55 μm	d , d_p , V_p	—	Application of La Vision Par- ticleMaster
(Anand et al. 2012)	2.3 $\mu\text{m}/\text{px}$	Dots on plate, 10–200 μm , LaVi- sion, mono-disperse droplets 135 μm	DOF correction	Area ratio at different thresholds	—	Fuel drop- lets, 10–200 μm	d_p	Mono-droplets: $< 1\%$, spray: $< 5\%$	Application of La Vision Par- ticleMaster
(Ju et al. 2012)	1.56 $\mu\text{m}/\text{px}$	Patterson globes, circles on plate, 18–145 μm	$< \pm 3$ mm	70% of DOF where interior area detectable	Linear	Glass spheres in water, 70–110 μm and 100–200 μm	d_p	—	Comparisons and advance- ments of (Kashdan et al. 2007; Yule et al. 1978)
(Robinson et al. 2012, 2013)	0.427 $\mu\text{m}/\text{px}$	PS particles dried on glass, 1–10 μm	100 μm , 1 μm	Image size and slope	—	Silica particles	d , d_p	d_p mean: 3.7–9%, d_p std.: 2.6–7% (for $d_p = 3$ –10 μm)	Analysis of Fresnel & Fraunhofer diffraction patterns
(Castanet et al. 2013)	5.5–7.5 $\mu\text{m}/\text{px}$	Dots on plate, 4–500 μm	± 1.5 mm, 100 μm	Contrast and gradient	Linear, two slopes, $d_p < \sim 25$ μm	Deflected spray drops, 116–171 μm	d_p , V_p	d_p : 4 μm if > 40 μm , else < 15 μm	Additional size correction, contrast only for small particles
(Legrand, Nogueira, Lecuona and Hernando 2016)	$\sim 0.43\times$, 15 $\mu\text{m}/\text{px}$	Dots on plate, 50–1000 μm by LaVision	-32 –36 mm, 1 mm	Contrast and gradient	Constant 10 mm for d_p 100–1000 μm		d , d_p	d_p : 10% up to $10 \times d_p$ from focus plane, else $< 20\%$, < 2 mm in positioning	Amount of rejected particles/dots relevant
(Minov et al. 2016)	8.23 $\mu\text{m}/\text{px}$	Monodisperse drop- lets, 119–497 μm	10 mm, 50 μm	Gradient, contrast	Linear, d_p dev. < 1 px	Spray: 24–543 μm	d_p , V_p	—	

Table 9 (continued)

Authors	Resolution/ magnification	Calibration object, sizes	Focus range, steps	In-focus crite- rion, based on	d - d_p -relation	Experimental object/sizes	Parameters (d_p , V_p , mass flow)	Error/ uncertainty	Remarks
(Warneke et al. 2017)	10 $\mu\text{m}/\text{px}$	Dots on plate, 10–2000 μm	–10–10 mm, 0.5 mm	Normalized gradient, image size	Function, in range ± 9 mm	Droplet breakup: 10–200 μm	d_p , V_p	d_p , V_p ; <4%	ITS detection code, d_{shadow} correction
(Hufnagel, Werner- Spatz, Koch and Staudacher 2018)	~0.88 $\mu\text{m}/\text{px}$	Dots on plate, 10–200 μm , LaVi- sion	DOF correction	ParticleMaster	Linear	Erosion in tur- bines Arizona Test Dust A3, 1–120 μm	d_p , mass flow	–	Application of La Vision Par- ticleMaster
(Senthilkumar et al. 2020)	1.2 $\mu\text{m}/\text{px}$	Bubbles and dots on plate, 20–400 μm	4 mm, steps 10 / 20 / 50 μm		Linear, based on number of found dots		d_p	$d_p = 63 \mu\text{m}$, <1–2%, general <5%	Comparison: calib. with bubbles vs. dots on plates, det. Particle number must be accounted
(Zhou, Tropea, Chen, Zhang, Luo and Cai 2020)	2.8 $\mu\text{m}/\text{px}$	Dots on plate, 30–240 μm	16 mm, ~100 μm	Two diam- eters of two cameras per particle	Linear	Spray, 50–250 μm	d_p , d	d_p ; <3–5%	Depth from defocus, two cameras, min. $d_p = 23 \mu\text{m}$
(Han et al. 2022)	1.7 $\mu\text{m}/\text{px}$	–	–	Gradient	Con- stant, ± 0.3 mm	Lime calcina- tion reactor: particles 15 μm –1 mm	d_p	–	min $d_p = 15 \mu\text{m}$, particle vol- ume concen- tration ~2%, no DOF calibration

Acknowledgements The authors would like to thank the mechanical team of Supersonic and Hypersonic Technologies Department for their mechanical and manufacturing support, as well as Patrick Seltner and Christian Hantz for their linguistic revision.

Author's contributions DA contribution to this work includes conceptualization, methodology, formal analysis, and investigation, original draft preparation as well as editing. DN contributed to review and technical expertise to this work. AG contributed to review, funding acquisition, resources, and supervision to this work.

Funding Open Access funding enabled and organized by Projekt DEAL. This work was fully funded by the DLR's Program Directorate for Space Research and Development in the frame of space transportation research activities.

Code availability For PTV and shadowgraphy image acquisition, DaVis 10.1.055537 from LaVision GmbH, Anna-Vandenhoeck-Ring 19, 37081 Goettingen, Germany, was used. For additional data processing, a custom code written in Python 3.8 was used, including common packages as well as:

Uncertainties: A Python package for calculations with uncertainties, v.3.1.5, Eric O. LEBIGOT, <http://pythonhosted.org/uncertainties/>, visited on 21.07.2021

Pco-tools, v1.0.0, <https://pypi.org/project/pco-tools/#files>, visited on 21.07.2021

ReadIM, v0.84, <https://pypi.org/project/ReadIM/>, visited on 21.07.2021.

Lvreader, v1.2.0, https://www.lavision.de/en/downloads/software/python_add_ons.php, visited on 30.07.2022.

Declarations

Competing interests The authors declare no competing interests.

Conflict of interest The authors have no relevant financial or non-financial interests to disclose.

Ethics approval Not applicable.

Consent to participate No special consent required for participation.

Consent for publication No special consent required for publication.

Open Access This article is licensed under a Creative Commons Attribution 4.0 International License, which permits use, sharing, adaptation, distribution and reproduction in any medium or format, as long as you give appropriate credit to the original author(s) and the source, provide a link to the Creative Commons licence, and indicate if changes were made. The images or other third party material in this article are included in the article's Creative Commons licence, unless indicated otherwise in a credit line to the material. If material is not included in the article's Creative Commons licence and your intended use is not permitted by statutory regulation or exceeds the permitted use, you will need to obtain permission directly from the copyright holder. To view a copy of this licence, visit <http://creativecommons.org/licenses/by/4.0/>.

References

Allofs D, Neeb D, Gülhan A (2022) Simultaneous determination of particle size, velocity, and mass flow in dust-laden supersonic flows. *Exp Fluids* 63. <https://doi.org/10.1007/s00348-022-03402-z>

Anand T, Mohan AM, Ravikrishna R (2012) Spray characterization of gasoline-ethanol blends from a multi-hole port fuel injector. *Fuel* 102:613–623

Bakum BI (1970) Characteristics of the working stream of hypersonic aerodynamic tubes in the presence of solid particle impurities. *J Eng Phys* 19:1290–1294. <https://doi.org/10.1007/BF00832671>

Castanet G, Dunand P, Caballina O, Lemoine F (2013) High-speed shadow imagery to characterize the size and velocity of the secondary droplets produced by drop impacts onto a heated surface. *Exp Fluids* 54:1489. <https://doi.org/10.1007/s00348-013-1489-3>

Chigier N (1991) Optical imaging of sprays. *Prog Energy Combust Sci* 17:211–262

Dehnadfar D, Friedman J, Papini M (2012) Laser shadowgraphy measurements of abrasive particle spatial, size and velocity distributions through micro-masks used in abrasive jet micro-machining. *J Mater Process Technol* 212:137–149. <https://doi.org/10.1016/j.jmatprotec.2011.08.016>

Dunbar L, Courtney J, Mcmillen L (1974) Heating augmentation in particle erosion environments 8th aerodynamic testing conference

Esser B, Koch U, Gülhan A (2006) Experimental and theoretical study of mars dust effects—heat transfer measurement report MDUST.

Fantini E, Tognotti L, Tonazzini A (1990) Drop size distribution in sprays by image processing. *Comput Chem Eng* 14:1201–1211

Fdida N, Blaisot J-B (2009) Drop Size Distribution measured by imaging: determination of the measurement volume by the calibration of the point spread function. *Measure Sci Technol* 21:025501. <https://doi.org/10.1088/0957-0233/21/2/025501>

Fleener W, Watson R (1973) convective heating in dust-laden hypersonic flows 8th thermophysics conference.

Ghaemi S, Rahimi P, Nobes DS (2010) Evaluation of stereopiv measurement of droplet velocity in an effervescent spray. *Int J Spray Comb Dyn* 2:103–123

Han S, Sun Z, De Jacobi Du Vallon C, et al. (2022) In-situ imaging of particle size distribution in an industrial-scale calcination reactor using micro-focusing particle shadowgraphy. *Powder Technol* 404:117459. <https://doi.org/10.1016/j.powtec.2022.117459>

Hovenac EA (1987) Performance and operating envelope of imaging and scattering particle sizing instruments

Hufnagel M, Werner-Spatz C, Koch C, Staudacher S (2018) High-speed shadowgraphy measurements of an erosive particle-laden jet under high-pressure compressor conditions. *J Eng Gas Turbines Power* 140

Ju D, Shrimpton JS, Hearn A (2012) A multi-thresholding algorithm for sizing out of focus particles. *Part Part Syst Charact* 29:78–92

Kapulla R, Tuchtenhagen J, Müller A, Dullenkopf K, Bauer H-J (2008) Droplet sizing performance of different shadow sizing codes. *Lasermethoden in Der Strömungsmesstechnik* 16:38–31

Kashdan JT, Shrimpton JS, Whybrew A (2003) Two-phase flow characterization by automated digital image analysis. Part 1: Fund Principles Calibration Technique. 20:387–397. <https://doi.org/10.1002/ppsc.200300897>

Kashdan JT, Shrimpton JS, Whybrew A (2007) A digital image analysis technique for quantitative characterisation of high-speed sprays. *Opt Lasers Eng* 45:106–115

Kim KS, Kim S-S (1994) Drop sizing and depth-of-field correction in Tv imaging. *Atomization Sprays* 4

Koh KU, Kim JY, Lee SY (2001) Determination of in-focus criteria and depth of field in image processing of spray particles. *Atomization Sprays* 11

Kudin OK, Nesterov YN, Tokarev OD, Flaksman YS (2013) Experimental investigations of a high-temperature dust-laden gas jet impinging on an obstacle. *TsAGI Science J* 44:869–884. <https://doi.org/10.1615/TsAGISciJ.2014011135>

Lavision GmbH G (2019a) Flowmaster Davis V10.1—product manual, pp 172

- Lavision GmbH G (2019b) Particemaster shadow—product manual. November 8, 2019b edn., pp 110
- Lebrun D, Touil C, Özkul C (1996) Methods for the deconvolution of defocused-image pairs recorded separately on two ccd cameras: application to particle sizing. *Appl Opt* 35:6375–6381
- Lecuona A, Sosa PA, Rodríguez PA, Zequeira RI (2000) Volumetric characterization of dispersed two-phase flows by digital image analysis. *Meas Sci Technol* 11:1152–1161. <https://doi.org/10.1088/0957-0233/11/8/309>
- Lee SY, Kim YD (2004) Sizing of spray particles using image processing technique. *KSME Int J* 18:879–894. <https://doi.org/10.1007/BF02990860>
- Legrand M, Nogueira J, Lecuona A, Hernando A (2016) Single camera volumetric shadowgraphy system for simultaneous droplet sizing and depth location, including empirical determination of the effective optical aperture. *Exp Thermal Fluid Sci* 76:135–145. <https://doi.org/10.1016/j.expthermflusc.2016.03.018>
- Minov SV, Cointault F, Vangeyte J, Pieters JG, Nuytens D (2016) Spray droplet characterization from a single nozzle by high speed image analysis using an in-focus droplet criterion. *Sensors* 16:218
- Molleson GV, Stasenko AL (2017) Gas-dispersed jet flow around a solid in a wide range of stagnation parameters. *High Temp* 55:87–94. <https://doi.org/10.1134/S0018151X1701014X>
- Niosh Pocket Guide to Chemical Hazards—Magnesium Oxide Fume. (2022). CDC—Centers for Disease Control and Prevention. <https://www.cdc.gov/niosh/npg/npgd0374.html>. Accessed 26.03.2022
- Nishino K, Kato H, Torii K (2000) Stereo imaging for simultaneous measurement of size and velocity of particles in dispersed two-phase flow. *Meas Sci Technol* 11:633
- Palmer G, Ching E, Ihme M, Allofs D, Gülhan A (2020) Modeling heat-shield erosion due to dust particle. *Impacts Martian Entries* 57:857–875. <https://doi.org/10.2514/1.A34744>
- Polezhaev YV, Repin IV, Mikhatulin DS (1992) Heat transfer in a heterogeneous supersonic flow. *High Temp* 30:1147–1153
- Putkiranta M, Eloranta H, Alahautala T, Saarenrinne P (2008) Droplet shadow sizing with a diode laser illumination and a depth-of-field calibration. In: ISFV13—13 th international symposium on flow visualization, July, 1–4, 2008, Nice, France. pp 11
- Robinson M, Mahmud Z, Swenson OF, Hoey J (2012) Development of a particle sizing algorithm for sub-10 μ m particles using shadowgraphy ASME International Mechanical Engineering Congress and Exposition. American Society of Mechanical Engineers, pp 899–906
- Robinson MJ, Mahmud Z, Swenson OF, Hoey J (2013) Sizing and positioning algorithm for 1 μ m to 10 μ m particles using shadowgraphy ASME International Mechanical Engineering Congress and Exposition. American Society of Mechanical Engineers, pp. V010T011A053
- Senthilkumar P, Mikhail S, Anand T (2020) Estimation of measurement error and depth of field in pdia experiments: a comparative study using water droplets and a calibration target. *Meas Sci Technol* 31:115204
- Vasilevskii E, Osipov A (1999) experimental and numerical study of heat transfer on a blunt body in dusty hypersonic flow 33rd thermophysics conference. American Institute of Aeronautics and Astronautics,
- Wang H, Felis F, Tomas S, Anselmet F, Amielh M (2017) an improved image processing method for particle characterization by shadowgraphy ilass-europe 2017 28th conference on liquid atomization and spray systems. pp 6
- Warncke K, Gepperth S, Sauer B et al (2017) Experimental and numerical investigation of the primary breakup of an airblasted liquid sheet. *Int J Multiph Flow* 91:208–224
- Yule A, Chigier N, Cox N (1978) Measurement of particle sizes in sprays by the automated analysis of spark photographs. *Particle Size Anal*, pp 61–73
- Zhou W, Tropea C, Chen B, Zhang Y, Luo X, Cai X (2020) Spray drop measurements using depth from defocus. *Measure Sci Technol* 31:075901. <https://doi.org/10.1088/1361-6501/ab79c6>

Publisher's Note Springer Nature remains neutral with regard to jurisdictional claims in published maps and institutional affiliations.